Extracting ECG-based cardiac information from the upper arm

by

Nargess Heydari Beni

A thesis

presented to the University of Waterloo

in fulfillment of the

thesis requirement for the degree of

Doctor of Philosophy

in

Systems Design Engineering

Waterloo, Ontario, Canada, 2022

Examining Committee Membership

The following kindly served on the Examining Committee for this thesis. The decision of the Examining Committee is by a majority vote.

External Examiner	Antti Vehkaoja Associate Professor Faculty of Medicine and Health Technology Tampere University
Supervisor	Ning Jiang Professor National Clinical Research Center for Geriatrics (WCH) West China Hospital, Sichuan University
Internal Member	Alexander Wong Professor Systems Design Engineering Department University of Waterloo
Internal-external	Arash Arami Assistant Professor Mechanical and Mechatronics Engineering Department University of Waterloo
External Member	Helen Chen Professor School of Public Health Sciences University of Waterloo
Defence Chair	Jennifer R. Whitson Associate Professor Stratford School of Interaction Design and Business University of Waterloo

Author's Declaration

This thesis consists of material all of which I authored or co-authored: see the Statement of Contributions included in the thesis. This is a true copy of the thesis, including any required final revisions, as accepted by my examiners.

I understand that my thesis may be made electronically available to the public.

Statement of Contribution

This thesis consists of three journal manuscripts written for publication (one already accepted) and one conference paper. My supervisor, Prof. Ning Jiang, has provided important contributions to all of these papers. The following credit statement holds for all three journal manuscripts and the conference proceeding:

Nargess Heydari Beni: Conceptualization, Methodology, Software, Formal analysis, Investigation, Data Curation, Writing (Original Draft), Visualization,

Ning Jiang: Conceptualization, Methodology, Validation, Resources, Writing (Review and Editing), Supervision, Funding Acquisition, Project Administration.

Citations:

Journal Manuscripts:

Chapter 3: N. Heydari Beni and N. Jiang, "Heartbeat detection from a single-lead ECG contaminated with simulated EMG at different intensity levels: a comparative study," *Biomed. Signal Process. Control*, Jan. 2023.

Chapter 4: N. Heydari Beni and N. Jiang, "Heartbeat Detection from High-Density EMG Electrodes on the Upper Arm at Different EMG Intensity Levels Using Zephlet," *SSRN Electron. J.*, Oct. 2022, available at SSRN 4221592.

Chapter 5: N. Heydari Beni and N. Jiang, "ECG delineation from the upper arm using mother wavelet optimization incorporated with Zephlet at four EMG contamination levels," not available online yet.

Conference Proceeding:

N. Heydari Beni and N. Jiang, "Heartbeat detection from the upper arm using an SWT-based zero-phase filter bank incorporated with a voting scheme," in *44st Annual International Conference of the IEEE Engineering in Medicine & Biology Society (EMBC)*, 2022.

Abstract

Cardiovascular Disease (CVD) is the global number one cause of death. Therefore, there is an acute need for constantly monitoring cardiac conditions and/or cardiac monitoring for extended periods. The current clinical Electrocardiogram (ECG) recording systems require precise placement of electrodes on the patient's body, often performed by trained medical professionals. These systems also have long wires that require repeated disinfection and can be easily tangled and interfered with clothing and garment. These limitations have severely restricted the possible application scenarios of ECG systems. To overcome these limitations, there is a need for wearable ECG devices with minimal wires to detect possible cardiac abnormalities with minimal intervention from healthcare professionals.

Previous research on this topic has focused on extracting cardiac information from the body surface by investigating various electrode placements and developing ECG processing algorithms. Building on these studies, it is possible to develop devices and algorithms that can extract ECG-related information without the need for precise electrode placements on the body's surface. The present thesis aims to extract ECG-based cardiac information using signals recorded from the upper arm.

Far-field ECG is prone to contamination by artifacts such as Electromyogram (EMG), which greatly reduces its clinical value. The current study examines how various state-of-the-art heartbeat detection algorithms perform in four levels of simulated EMG artifacts. The

simulated EMG was added to Lead II from two different datasets: the MIT-BIH arrhythmia dataset (Dataset 1) and data we collected from 20 healthy participants (Dataset 2). Results show that Stationary Wavelet Transform (SWT) provided the most robust features against EMG intensity level increment among various algorithms. The next step involved recording bio-potential signals using a high-density bio-potential amplification system attached to the upper arm. The system used three high-density electrodes, each with 64 channels, in addition to the standard Lead II. Twenty participants, reported healthy, were asked to perform two tasks: Rest and Elbow Flexion (*EF*): holding three weights (C_1: 1.2 kg, C_2: 2.2 kg, and C_3: 3.6 kg). The tasks were repeated 2 and 3 times, respectively. Firstly, I identified optimal electrode locations on the upper arm for each task. I then generated a synthesized ECG using the selected electrodes with generalized weights over subjects and trials. Considering the robustness of SWT to EMG intensity level increment, I next focused on optimizing SWT by addressing two of its drawbacks: introducing phase shift and the requirement of a pre-defined mother wavelet. Regarding the first drawback, zero-phase wavelet (Zephlet) was implemented to replace SWT filters with zero-phase filters for the matter of feature extraction from the synthesized ECG. Next, I incorporated the synchronized extracted features with a Multiagent Detection Scheme (*MDS*) for the means of heartbeat detection. The F1-score for the heartbeat detection was 0.94 ± 0.16, 0.86 ± 0.22, 0.79 ± 0.26, and 0.67 ± 0.31 for Rest and *EF* with three different levels of muscle contraction (C_1 to C_3), respectively. Changing the acceptable distance between the detected and actual heartbeats from 50 ms to 20 ms, the F1-score changed to 0.81 ± 0.20,

0.66 ± 0.26, 0.57 ± 0.26, and 0.44 ± 0.26 for Rest and C_1 to C_3, respectively. Regarding the second drawback, Lattice parametrization was used to optimize the mother wavelet for the means of PQRST delineation. The mother wavelet was generalized over subjects, trials, and tasks. The Pearson's Correlation Coefficient (CC) between the averaged delineated PQRST from analyzing feature and the averaged PQRST from Lead II using this generalized mother wavelet was 0.88 ± 0.05, 0.85 ± 0.08, 0.83 ± 0.11, and 0.81 ± 0.12 for Rest and C_1 - C_3, respectively.

This thesis makes several contributions to the current literature. It introduces locations on the upper arm that can be used to place sensors in a wearable to capture cardiac activity with robustness across intra-subject, inter-subject and inter-contraction variabilities. It also identifies a robust method against noise increment for heartbeat detection. Zephlet was implemented for the first time that can replace SWT in many applications in which there is a need for synchrony with respect to the original signal or among components. And finally, this thesis introduces a generalized mother wavelet that can be used to extract PQRST and enhance SNR in many applications, such as ECG waveform extraction, arrhythmia detection, and denoising.

Acknowledgements

First, I would like to thank my supervisor, Prof. Ning Jiang. He took the time and effort to help make this thesis the best it could be for over four years. I could not have made it this far without his guidance and support.

I would also like to thank the members of my dissertation committee - not only for their time and extreme patience but for their intellectual contributions to my development as a scientist.

I also want to express my sincerest gratitude to all my participants for the time they took to participate in my experiment.

To my friends Elham Mohammadi, Davood Adineh, Fatemeh Karimi, Hossein Sonbolestan, Nahal Ramezani, Ashirbad Pradhan, Ana Lucia Diaz De Leon Derby, and everyone who made a family for me here: I could not have done this without you!

Last but certainly not least, my deepest gratitude goes to my lovely partner, Rory Ewing, for his amazing and unconditional kindness and support.

Dedication

I wholeheartedly dedicate this thesis to my family, Maryam Sharif Samani, Behnam HeydariBeni, Nasimeh HeydariBeni, and Mahdi Soleymani, who endured my absence so that I could study at the University of Waterloo. There are no words to express how grateful I am for you. Your support and inspiration made me believe in myself, be resilient, and fight for my dreams. I am truly blessed and honoured to have you as my family.

Table of Contents

xiii

xiv

List of Figures

xviii

List of Tables

List of Equations

List of Abbreviations

CVD: Cardiovascular Disease
ECG: Electrocardiogram
SNR: Signal-to-Noise Ratio
EMG: Electromyogram
SWT: Stationary Wavelet Transform
ICA: Independent Component AnalysisBL: Baseline
EF: Elbow Flexion
MDS: Multiagent Detection Scheme
SA: Sinoatrial
AV: Atrioventricular
MVC: Maximal Voluntary Contraction
PCA: Principal Component Analysis
FFT: Fast Fourier Transform
EMD: Empirical Mode Decomposition
WT: Wavelet Transform
CWT: Continuous Wavelet Transform
DWT: Discrete Wavelet Transform
IMF: Intrinsic Mode Function
EEMD: Ensemble Empirical Mode Decomposition
CEEMDAN: Ensemble Empirical Mode Decomposition with Adaptive Noise
STFT: Short-Time Fourier Transform
STD: Standard Deviation
CC: Correlation Coefficient
MVR: Multivariate Regression
MRA: Multiresolution Analysis

Chapter 1

Introduction

Cardiovascular Disease (CVD) is the number one cause of death globally. Approximately 50 percent of these deaths are caused by lethal arrhythmias [1]. Accurate recording and detection of a variety of cardiac arrhythmias are essential in preventing death due to these conditions. Abnormal transient heart activities may not occur during an individual's hospital visit. Hence, cardiac conditions need to be monitored for many people, preferably outside of clinical institutions and in an environment of their normal daily activities, either constantly or for extended periods. The COVID-19 crisis further accentuates this requirement. In many jurisdictions, healthcare authorities mandated that non-critical cardiac patients be sent home to reserve clinical resources and prevent these patients from infection by COVID-19. Further, more recent epidemiology studies found that people infected by COVID have a significantly higher risk of developing cardiovascular disease. As such, cardiologists need advanced tools to continuously monitor patients' conditions so that they would be less vulnerable to serious and often fatal cardiac events. Ideally, abnormal cardiac events should be detected as quickly as possible so that proper medical attention can be provided at the earliest opportunity [1]. Accordingly, automatic detection of arrhythmias is required [2].

Electrocardiogram (ECG) is the most widely adopted clinical tool that provides a graphical representation of the electrical activity of the heart from the body's surface. This electrical activity determines the rate and rhythm of the cardiac electric activities. Physicians

1

routinely use the recorded information using ECG for CVD conditions diagnoses such as cardiac arrhythmias, myocardial infarctions, atrial enlargements, ventricular hypertrophies, and bundle branch blocks. In order to provide consistent ECG signals, trained professionals have to precisely place the electrodes on standard positions on the chest and upper and lower extremities for registration of clinical-grade ECG. However, even professional nurses make mistakes when placing ECG electrodes, let alone laymen. Furthermore, although the ECG signals on the chest have sufficient amplitude to allow clinical-grade quality, the required electrode placements are not comfortable, especially while sweating and in long-term monitoring. The wires connecting the electrodes and the amplifying unit are long, cumbersome, hazardous, and need constant disinfection [3][4]. Therefore, current ECG systems suffer from inconveniency, distributed sensors, additional wires, and low wearability [5]. Furthermore, the clinical ECG system is not designed to be used at home, and no alternative ECG system is available for these patients to monitor their cardiac conditions at home. Some studies in the literature focus on designing ECG devices with non-standard ECG lead configuration to enhance the wearability, convenience, comfortability, reusability, and the possibility of being used for home-based measurements (see a review in [6]). Ideally, such a device should be able to provide continuous ECG acquisition without the supervision of a healthcare professional.

One of the most challenging aspects of using a wearable system for cardiac abnormality identification is precise ECG delineation from the recorded signals. The reported studies can be summarized as focusing on two main areas: the choice of alternative electrode placement and the development of ECG processing algorithms.

In terms of alternative electrode placement, studies have investigated locations such as finger [7], wrist [8], [9], ear [5], and arm [5], [8], [10]–[12]. However, these positions all have drawbacks. For instance, registration of the ECG signals from the finger or two-wrist configurations requires crossing hands/wrists [12]. A device utilizing ear, wrist, and finger locations may suffer from low wearability and physically separated sensors [5]. Alternatively, the electrode placement on the left arm does not require attaching the separate ECG electrodes to different body sites. This advantage is achieved by leveraging the high signal-to-noise ratio (SNR) and bipolar electrodes attached to different positions on the left upper arm. This placement also improves wearability and comfort in long-term daily applications [12]. However, the desired automatic mechanism of abnormality detection should be continuous and with minimal involvement from the user, which is missing in the related studies in the literature.

In terms of the second approach, *i.e.*, ECG processing algorithms, many studies have proposed different algorithms to extract electric information pertaining to cardiac activity from the registered signals over the body, including standard [13]–[16] and non-standard [1],

3

[17][18] electrode placements. In far-field ECGs, the amplitude of Electromyogram (EMG) and other interfering sources becomes more comparable to ECG, so SNR is considerably lower. The interpretation enhancement and diagnosis have been explored in different aspects of ECG signal processing, such as denoising [17]–[19], extracting different features [20]–[23], investigating multi-lead ECG [24]–[27], and detecting possible arrhythmia [2], [28]–[30]. Among ECG waveforms, the QRS complex is the most pronounced having a significantly large amplitude of R-peak. Hence, the detection of QRS complexes plays a fundamental role and is routinely used as the first step in heartbeat detection [19]. Accurate detection of QRS complexes is therefore critical prior to ECG processing [20], and it can further lead to the identification of cardiac arrhythmias [2]. In summary, the extracted signals in most of the studies in the current literature are not clinical-grade ECG, or the intended applications are not medical applications, or they are expensive and restrictive and not available to a large population that would benefit from them.

In this thesis, my goal was to extract ECG-based cardiac information from non-conventional locations on the body's surface to be further used in a wearable device. This device can address the difficulty and usage restrictions of standard ECG recording systems on a daily basis.

A wearable device on the upper arm that continuously monitors cardiac activity has several advantages over existing devices such as ECG Holter monitors, adhesive patches, and

Apple Watch. ECG Holter monitors can record data for a maximum of a few days, and they can be uncomfortable for many users [21]. Adhesive patches can be used for short- to mid-term monitoring applications (up to one week or intermittently over an extended period). Moreover, they can be uncomfortable and allergen to some users [21]. In addition, adhesive patches are not big enough to cover all the standard ECG leads, but it is expected for a wearable on the upper arm to contain that information (considering different locations). Furthermore, the electrode placement on the upper arm provides a higher SNR compared to other non-conventional locations (*e.g.* ear or wrist) and higher wearability and comfort. In a wearable device on the wrist, such as the Apple Watch [18], the users need to put their fingers of the opposite hand on the watch, which is not possible to perform continuous recording and is also not feasible for all users.

However, there are some challenges with such a device as well. Due to the distance from the heart and low SNR of the upper arm signals compared to conventional ECG, real-time extraction of cardiac information with high accuracy and minimal latency is the main challenge. It was crucial to design and implement automated and real-time (or with the capacity of performing in real-time) algorithms in this thesis with minimal or no supervision requirement. The study design tried to replicate a real-world scenario covering various SNR levels and activity intensities yet be generalized and robust. Furthermore, not only the

performance of the algorithms in various SNR levels was important, but also reducing the latency of the system was highly critical.

There are several research questions that I address in this thesis. The main research question is whether it is possible to extract ECG-based cardiac information from the upper arm. I targeted heartbeat locations and ECG morphology as the desired cardiac information. The research question then expands to more detailed questions:

- What locations on the upper arm are the best to place the electrodes and extract ECG-based cardiac information?

- How can we extract robust features to get high-performing heartbeat detection while the signal is contaminated with muscle activity at various intensity levels?

- Is it possible to detect heartbeats from the upper arm?

- How can we improve the heartbeat detection performance of a robust algorithm against muscle activity levels?

- Is it possible to delineate ECG morphology from the upper arm undergoing various muscle activity levels?

- How can we generalize the ECG morphology delineation method across intra-subject, inter-subject and inter-contraction variabilities?

The current chapter provides a brief literature review and introduces the motivation of the thesis. The in-depth literature review and background are given in Chapter 2, including the

required information and preliminary knowledge about recording bio-signals from the body surface and some existing techniques to extract the ECG from the registered information and the removal of interfering signals. Chapter 3 provides a comparative study with the objective of identifying a high-performing and robust pipeline for heartbeat detection using different feature extraction methods from single-lead ECG contaminated with simulated EMG at four intensity levels. I tried to implement state-of-the-art and popular methodologies for feature extraction and then challenged them at high to very high low SNR levels. It made it difficult to compare the results to the existing literature because, to the best of my knowledge, studies do not cover those low levels of SNR while implementing heartbeat detection algorithms. Chapter 4 presents a novel approach to heartbeat detection from the upper arm, with the objective of selecting the optimized location of electrodes on the upper arm to provide the most information regarding ECG. This selection was made for four EMG intensity levels with consideration of generalization purposes. I then generated a synthesized ECG using the selected electrodes for further processing steps. The secondary objective was to accurately detect heartbeats from the synthesized ECG at each EMG intensity level. Toward this objective, I optimized the identified feature extraction method from chapter 3 by addressing one of its drawbacks. By addressing another drawback of this method, I further optimized it for ECG morphology delineation in Chapter 5. Chapter 6 concludes the previous chapters' results and discusses the challenges and future work.

This thesis makes several main contributions to the current literature, as follows:

- Introducing optimal locations on the upper arm that can be used to place sensors in a wearable to capture cardiac activity with robustness across intra-subject, inter-subject and inter-contraction variabilities.

- Identifying a robust method against noise increment for heartbeat detection.

- Implementing Zephlet for the first time that can replace SWT in many applications in which there is a need for synchrony with respect to the original signal or among components.

- Introducing a generalized mother wavelet (across intra-subject, inter-subject and inter-contraction variabilities) that can be used to extract PQRST and enhance SNR in many applications, such as ECG waveform extraction, arrhythmia detection, and denoising.

Chapter 2

Background and Literature Review

This chapter provides an introduction to ECG and other sources that are present in the recordings from the upper arm. Furthermore, widely used methodologies for interpreting information pertaining to cardiac activities from recorded signals are introduced.

The signals that are present in a recording from the upper arm can be categorized as ECG (desired) and noises and artifacts (undesired). The noises and artifacts category includes power-line interference, electrode contact noise, baseline wanders, and EMG. More details about these signals are represented as follows:

2.1 ECG

The cardiovascular system consists of three main components, the heart, the blood vessels, and the blood. The heart functions as a pumping station consisting of two pumps: the right and the left side of the heart. Each side has one chamber for receiving the blood (atria) and another chamber for moving the blood away from the heart towards body organs through the vessels (ventricles). The pumping function is dependent mostly upon the contraction (systole) and relaxation (diastole) properties of the myocardium. The contraction of the myocardium occurs when an electrical stimulation, which is higher than a threshold, applies to the cell. The rapid electrical change in the cell results in the movement of ions across its plasma

membrane. Increasing the voltage difference between the interior of the cell and the extracellular fluid from approximately -90 mV to 20 mV is called depolarization. After a short period (<0.3s), the changes in the membrane result in repolarization, which is the restoration of the original ionic balance in the cells. This entire electrical event of rapid potential polarity change across the plasma membrane is called a cardiac action potential [22].

Some cardiac cells function as pacemakers by posing the property of the automaticity that provides spontaneous depolarization. Moreover, myocardium cells have the property of transmitting action potentials from one cell to adjacent cells. Therefore, when a rhythmic pacemaker within the heart generates an action potential, it is conducted throughout the organ and results in a coordinated contraction. This contraction triggers the pumping process and results in a mechanical heartbeat. The activation wave in the atria initiates in the Sinoatrial (SA) node, which results in moving blood from the right atria to the right ventricle and from the left atria to the left ventricle at the rate of 1 m/s. The activation wavefront then moves to the atrioventricular (AV) node, in which the rate slows down to 0.5 m/s to allow time for the ventricles to fill with the blood from the atria. After the AV node, the wavefront reaches the Purkinje system, which spreads very rapidly (at almost three m/s) to many cells in both ventricles, and simultaneous contraction of both ventricles occurs. So, the blood moves from the right and the left ventricles out to the pulmonary and systemic circulation, respectively (Figure 2-1) [22][23].

The electrical activity of the cells produces an electromagnetic field that establishes a changing potential field on the surface of the skin that can be measured and amplified using suitable equipment. The resultant recording signal of these surface potentials as a function of
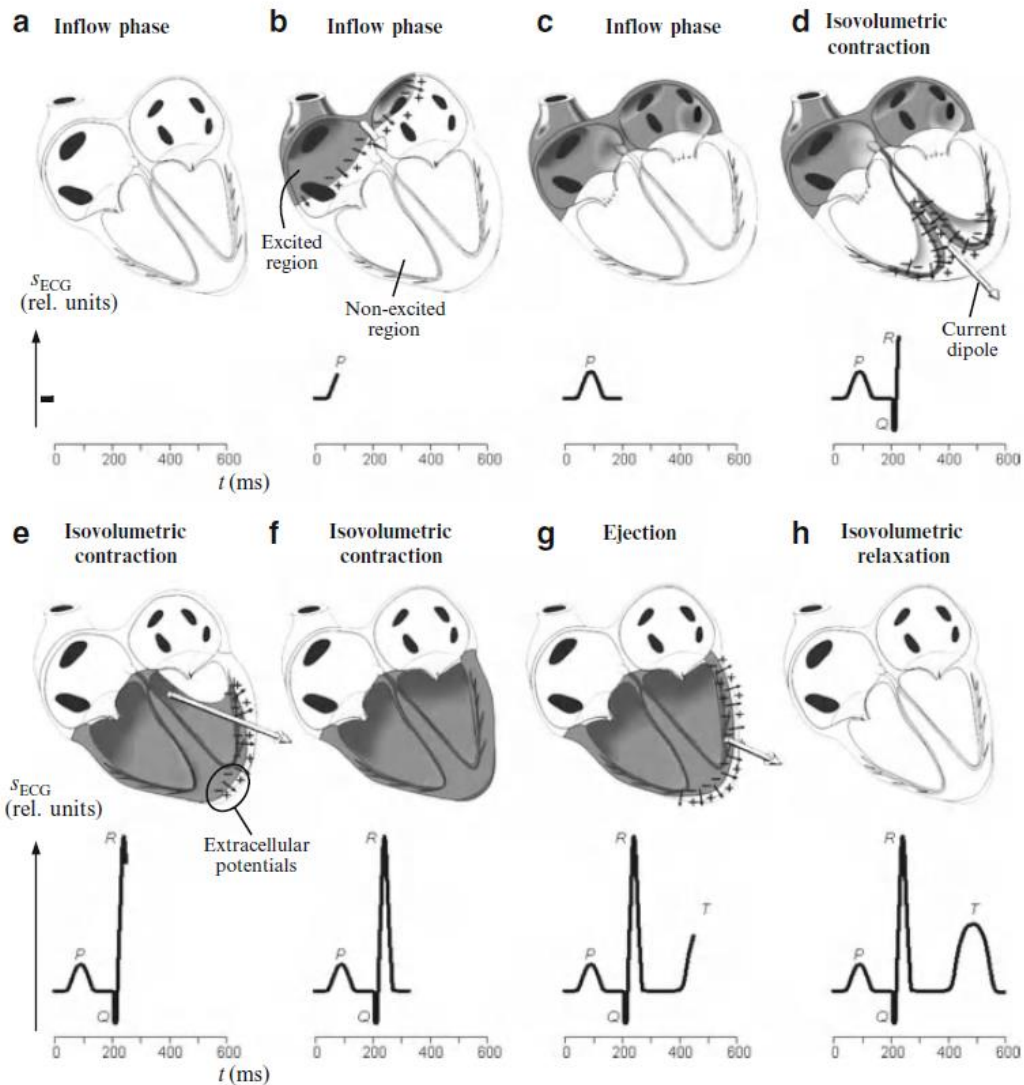
Figure 2-1. Electrical excitation of the heart propagating from atria to ventricles which results in ECG pattern generation.

time produces the ECG signal (Figure 2-2) [23]. The P wave represents the atrial depolarization, and the QRS complex represents the depolarization of the ventricles. Atrial repolarization is masked by ventricular depolarization, while ventricular repolarization shows up as the T wave, as illustrated in Figure 2-2 [22]. There are four main hypotheses about the source of U-wave: repolarization of the intraventricular conducting system or Purkinje fibres system, delayed repolarization of the papillary muscles, afterpotentials caused by mechanoelectrical hypothesis or mechanoelectrical feedback, and the prolonged repolarization in the cells of the mid-myocardium ("M-cells") [24].
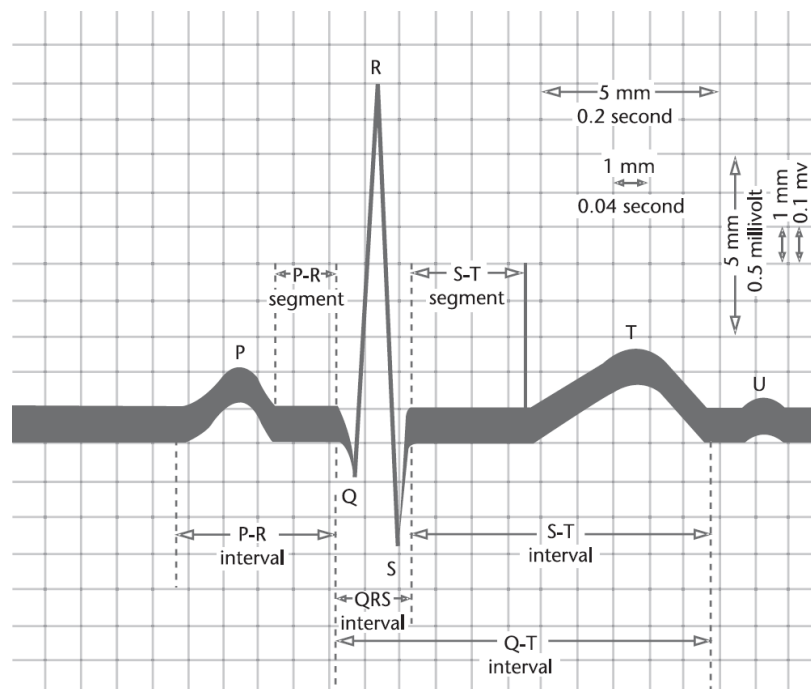
Figure 2-2. Normal features of ECG including P-wave, QRS complex, and T-wave.

Any disorder in the heart rate, rhythm, or morphological pattern change should be detected by observing ECG waveform and indicates an arrhythmia [25].

2.2 Noises and Artifacts

The first step for extracting reliable features from ECG is signal conditioning, which aims to reduce the interfering signals that are generated by sources other than the heart. These sources can be physiological or non-physiological, which are known as artifacts and noises, respectively. Encountered noises are mainly categorized as power-line interference and electrode contact noise, and the most significant artifacts include motion artifacts and muscle contractions (EMG). Moreover, the baseline wander is another interfering source, containing both noise and artifact components. These undesired components are described in more detail as follows:

2.2.1 Power-Line Interference

The cables carrying the recording signals are affected by the electromagnetic interference of power supply lines with a frequency of 50 or 60 Hz. This contamination is a significant source of noise for ECG signals. Although the power-line noise has a frequency of 50 or 60Hz, it has a finite bandwidth around the center frequency in reality [26], which is important in denoising. Notch filtering at 50 Hz or 60 Hz or bandpass filtering with the upper cut-off frequency below these values has been a common choice for reducing the power-line noise [27][28].

2.2.2 Electrode Contact Noise

loss of electrode contact with skin causes sudden changes in the magnitude of the recording signal, overwhelming any ECG components. The sudden changes induce dramatic transients in the baseline, which decay exponentially to the baseline values [27]. The resulting poor conductivity reduces the ECG amplitude and SNR and increases the possibility of disturbances.

2.2.3 Baseline Wander

A diversity of sources can cause baseline wandering, such as patient's movement, breathing, movement of cables, dirty electrodes, and variation in skin-electrode impedance caused by electrode motion. This type of noise is more significant during exercise ECG, and the frequency range is typically below 1Hz. High-pass filtering [28], ICA [29], and Principal Component Analysis (PCA) [30] are routinely used in the literature to reduce the effects of these sources on ECG recordings.

2.2.4 EMG

The electrical signals travelling between skeletal muscles and the nervous system control the movement and position of limbs. The EMG is the registration and interpretation of skeletal muscle potentials. The EMG signal has physiological origins in individual fibres (contractile units within a muscle) or groups of muscle fibres and is affected by their feature variation. The

muscle features differ among muscles and within or among individual subjects; features such as muscle fibre length and fibre type composition variation, muscle partitioning, and variation in the distribution of sensory receptors.

A motor unit consists of muscle fibres and the motor neuron that innervates them. It is the smallest independently functioning muscular system unit, and the EMG signal is the summation of the action potentials generated by many motor units. These potentials occur at random times, producing an interference pattern similar to noise [31]. Because the motor units act randomly and independently, the EMG can be considered a stochastic process. Contrary to a deterministic process, future values cannot be precisely predicted in the stochastic process. However, they follow a probabilistic pattern. The probability distribution is the mathematical description of the relative likelihood of possible EMG amplitude. Moreover, the number of active motor units is large, so the probability distribution of their summation, which is registered as the EMG, can be considered Gaussian distribution. This distribution is dependent on the strength of muscle contraction and is more Gaussian-shaped when the contraction intensity approximately equals 70% of the Maximal Voluntary Contraction (MVC) [32].

Moreover, the frequency range of EMG is typically between 6 and 500 Hz having the most power between ~20 and 150 Hz [33]. Knowledge about these characteristics of EMG leads to a better understanding of analyzing and filtering this type of bio-signal.

In contrast to other contaminating components, removing EMG from ECG presents a much more challenging problem since its spectral content considerably overlaps that of the ECG signal. In far-field ECGs (not recorded from the chest or standard leads), the amplitude of EMG and other interfering sources mentioned above becomes more comparable to ECG, so SNR is considerably lower. Subjects with tremors, kids, or those afraid of ECG recordings also usually have higher EMG signals. The comparison of the SNR of the best recordings from the chest, bipolar arm (transversal), and bipolar wrist (longitudinal) channels has distinctly shown this reduction, as shown in Table 1 [34].

In the following, ECG feature extraction methods that have been used to enhance the SNR of recorded ECG signals and suppress undesired sources, especially EMG, are reviewed.

.

Table 1. SNR mean values (in dB) along chest, upper arm, and wrist for six recording cases

Subject	Chest	Upper Arm	Wrist
1	20.97	1.27	0.48
2	13.75	4.93	1.81
3	55.29	36.86	1.85
10	60.59	197.05	2.15
17	37.68	1.49	0.16
36	98.85	3.67	4.99
Mean	**47.85**	**40.88**	**1.91**

16

2.3 ECG Feature Extraction Methods

Investigating the signal conditioning techniques to reduce the noises and artifacts is a continuing concern within far-field ECG research. Removing EMG as the most significant artifact from ECG presents the most challenging problem since its spectral content (6-500 Hz) completely overlaps that of the ECG signal (0.5-100 Hz). In addition, when the user performs a physical activity and the activated muscles are in the vicinity of the ECG electrodes, the EMG contamination will overwhelm the ECG waveforms. Therefore, EMG can considerably affect the performance of heartbeat detection algorithms and subsequent identification of P-QRS-T complex characteristics.

Many temporal, spectral, and spatial ECG feature extraction methods can be used to enhance the SNR of recorded ECG signals and extract the features which can lead to the detection of different ECG patterns, especially QRS complex. The most striking ECG waveform is the QRS complex, which plays a fundamental role in automated heart rate determination and abnormality identification [35].

The most commonly used feature extraction techniques to increase the SNR in single-channel ECG are represented as follows:

2.3.1 Ensemble Averaging

Since ECG is a repetitive signal, similar techniques to processing evoked potentials in Electroencephalogram (EEG) analysis can be applied [36]. So, ensemble averaging over beats

17

is a successful information enhancement method; however, it causes latency in the denoising stage as it requires several real-time beats to extract one particular PQRST morphology [8]. Besides, QRS timing detection as a pre-stage is a challenging concept and plays an important role in denoising.

2.3.2 Algorithms based on Amplitude and its Derivatives

Amplitude is known as the oldest feature used to detect R-peaks in ECG signals [37][38]. It is mostly followed by a differentiator to reduce the influence of T-wave and P-wave relative to R-wave [39]. First and second-derivative algorithms function as high-pass filters, which can be beneficial, considering the steep slope of the R wave. The researchers have implemented them separately [40][41], and with a linear combination [42] followed by methods such as thresholding for the detection stage.

2.3.3 Filter Banks

Considering the frequency range of EMG between 6 and 500 Hz with the most power between ~20 and 150 Hz, filtering some frequency components that are not of interest will help with achieving a cleaner ECG signal. However, the Butterworth lowpass filtering with cut-off frequencies such as 15 [11], 30 [7], and 35 Hz [43] is limited in EMG artifact suppression and considerably affects the QRS complex slopes [43].

2.3.4 EMD

EMD was introduced by [44] as an adaptive and fully data-driven technique. It extracts oscillatory modes embedded in the data. In EMD, the basis used in the analysis is generated by the same analyzed signal. Therefore, there is no need to set *a priori* level of decomposition, which is an advantage over other decomposition techniques. EMD decomposes signal to a variable number of components or Intrinsic Mode Functions (IMFs). IMFs are dynamic and consist of different frequency components. The initial IMFs convey high-frequency information, and higher-order IMFs express low-frequency information, considering the nature of component extraction [45]. Among ECG waveforms, the QRS complexes have higher frequency content compared to P- and T-waves (3-40 Hz vs. 0.7-10 Hz). Therefore, they are expected to be captured in earlier IMFs compared to P- and T-wave [46][38]. For instance, Kozia et al. used the first three IMFs for reconstruction, which includes the frequency range of 3-40 Hz as the components containing the QRS complex [46].

When the ECG signal is contaminated with EMG, because EMG includes frequency content in the range of 6-500 Hz, the initial IMF(s) are expected to include EMG-related information rather than QRS complexes [47][48], and then some of the higher order IMFs would include QRS complexes. It needs to be mentioned that IMFs that capture QRS complexes will also have EMG-related information (due to frequency overlap) [49]. Removing unwanted sources can be done by partially reconstructing the original signal (by selecting a

19

subset of IMFs; and desired frequency range of 0.5-30 Hz) or applying post-processing methods such as Fast Fourier Transform (FFT) [10] or Wavelet Transform (WT) [48][50] on the IMFs. Furthermore, thresholding techniques applied to a subset of IMFs as a noise removal step are proven to effectively enhance R-peak detection for different ECG shapes [51].

There are also some studies that use EMD first to convert single-channel ECG into several components and then apply Independent Component Analysis (ICA) to enable heartbeats extraction from the resulting independent components [52], [53]. This way, the EMD algorithm first decomposes the signal into spectrally independent modes and then ICA extracts statistically independent sources [54].

Empirical Mode Decomposition (EMD) suffers from similar oscillations across different modes, which is called mode mixing. If the amplitudes and frequencies of the signal and noise do not have enough difference, mode-mixing happens. Wu et al. proposed a new method called Ensemble Empirical Mode Decomposition (EEMD) to overcome this issue [55]. EEMD applies EMD to an ensemble of white Gaussian noises added to the signal to solve the mode mixing problem. Although EEMD has been useful in many signal processing applications [56]–[58], it also suffers from some limitations. First, the ensemble averaging cannot completely eliminate the artificially added Gaussian noise. Furthermore, each realization can produce a different number of modes, which makes it difficult for the subsequent averaging

operation. An improved method called Complete Ensemble Empirical Mode Decomposition with Adaptive Noise (CEEMDAN) was proposed to resolve these limitations [59].

In terms of computational load, it should be considered that EMD consists of at least nine processing steps. The resulting computational load is more than the amplitude, derivative-based, and filter bank techniques [60]. The computational cost of EEMD is considerably higher than EMD. On the other hand, CEEMDAN needs a lesser number of siftings than EEMD and consequently a lower computational cost, but still considerably higher than EMD. Furthermore, another drawback of all EMD-based methods is that there is no model to be trained, and the obtained components from unseen data with non-stationarity could lead to inconsistent results.

2.3.5 WT

Fourier analysis provides power decomposition with respect to each frequency component. However, it assumes the temporal stationarity of the signal to be analyzed and removes all temporal structure information within the signal, which is essential for ECG processing. As a compromise, the Short-Time Fourier Transform (STFT) only assumes stationarity within the analysis window and performs Fourier analysis on the windowed data segments. When the temporal structure of interest is comparable to the length of the analysis window, STFT can be a reasonable tool. When the temporal structure changes in the signal, the fixed length in the analysis windows of STFT becomes inadequate. By using a set of

analyzing functions, WT provides variable time-frequency resolution for different frequency bands [38]. The analyzing (basis) functions result from scaling and translating a mother wavelet, which has values in a certain temporal range and zeros elsewhere. As one type of WT methods, Continuous Wavelet Transform (CWT) projects a continuous signal to a continuous family of frequency bands that enables us to observe the frequency information at any given time. The CWT allows the scaling and translating parameters to vary continuously rather than discretely, which results in an overcomplete representation of the signal. The Discrete Wavelet Transform (DWT), on the other hand, discretizes parameters of the basis functions, which significantly reduces the redundancy of CWT. In DWT, the scale parameter is a power of 2, and the translation parameter has non-zero positive integer values. In ECG processing literature, there are various approaches to detect the QRS complexes from ECG through DWT.

Information about each ECG waveform is presented in the wavelet coefficients or the sub-bands containing the corresponding frequency content. Studies have used different decomposition levels in DWT and have assumed the QRS complex to be characterized in a subset of details based on their frequency content, including details 1-4 (overall frequency content of 11.25-180 Hz) [61], [62], 3-5 (5.75-45 Hz) [2], 4 (15.6 -31.1 Hz) [63].

The singularities (sharp edges or spikes) in the signal result in pairs of modulus maxima across several scales, as illustrated in Figure 2-3. Hence, some of the studies which use DWT as the feature extraction method have investigated peakiness or singularity degree calculation

for peak detection [64][65]. Moreover, the selection of wavelet coefficients in which the QRS complex is dominant provides a signal with higher SNR, which results in being more robust to noise [38].

DWT has been very popular in ECG denoising since it satisfies the energy conservation law and provides perfect reconstruction. The solid mathematical basis of DWT results in robust statistical analysis and efficiency in computational cost compared to EMD [66]. However, the studies that have chosen EMD over DWT for QRS detection have addressed the problem of
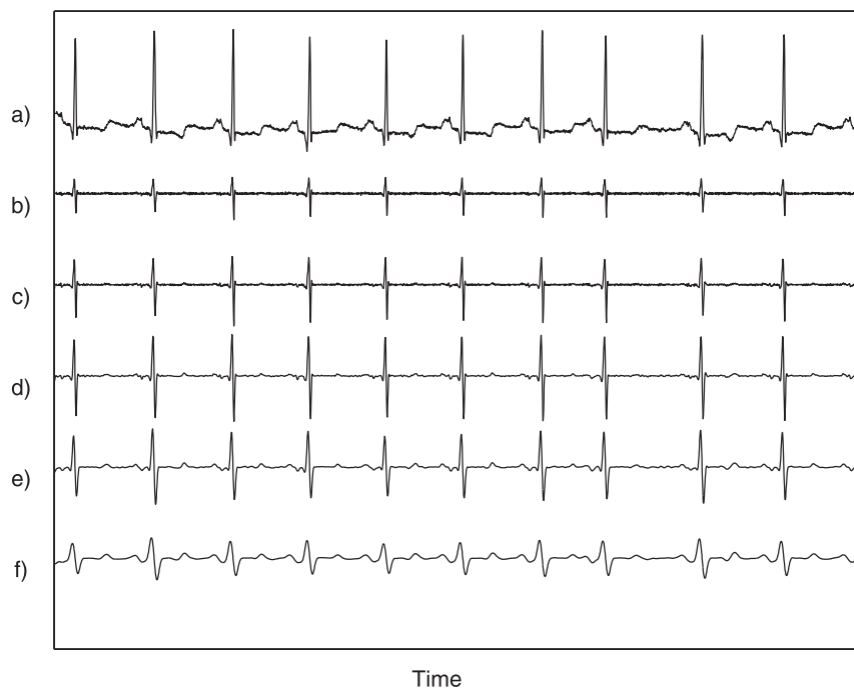
Figure 2-3. ECG signal(a) and Corresponding wavelet coefficients in the scales 1(b) to 5(f). The paired modulus maxima present across all the scales synchronized with the QRS complex.

23

mother wavelet selection as their motivation to avoid using DWT [67][47]. Besides, deriving the basis functions from the signal itself results in a data-driven adaptivity, contrary to DWT, which uses fixed basis functions and requires a fixed number of decomposition levels in prior [66][47]. More recently, some studies have focused on combining DWT and EMD, providing complementary features [68].

Stationary Wavelet Transform (SWT) was further introduced to address DWT drawbacks, such as shift sensitivity and loss of temporal resolution at rough scales. The down-sampling in DWT means that the length of the coefficients at level N is 2^{-N} times the length of the original signal, which results in losing resolution in higher scales. On the contrary, in SWT, the filter coefficients are up-sampled in each level of SWT. Consequently, the resulting coefficients have the same length as the original signal. Therefore, SWT is shift-invariant since its representation is redundant. Consequently, it is applicable for accurately locating an event of interest in a signal, such as an edge [20][69]. Furthermore, studies have represented SWT as a leading technique to increase SNR [70][71]. Kumar et al. have claimed SWT is the best available ECG denoising technique in a recent study comparing some denoising methods, including SWT, DWT, and EMD [71]. Furthermore, the accuracy of extracted features from SWT has proven to outperform those of EEMD in studies focused on EEG analysis [71]. In a recent study, Dwivedi *et al.* studied contaminated ECG signals by powerline interference (PLI) noise and then proposed a denoising method by combining SWT and EEMD. After applying

EEMD and removal of the first IMF, they used three-level SWT, selected several detail coefficients, and reconstructed a signal with higher SNR [71].

However, while SWT provides decent robustness against noise and is a relatively straightforward method, it has two main particular disadvantages: it alters the original signal phase [8] and requires a pre-defined mother wavelet [71]. The first drawback, phase shift, is the result of using FIR filter banks with non-zero phases in the wavelet decomposition schemes. As a result of this phase shift, the QRS complexes are projected in different temporal locations at different levels of SWT detail coefficients, all of which are different from their original positions. The shift is confined to milliseconds and is problematic and obviously undesirable in the application of QRS detection. Due to the phase shift propagating across the SWT scales, the shift is expected to get larger as the scale grows. Thus, the last detail and approximation will exhibit the greatest phase shift compared to the original input signal. Consequently, more information may be lost on higher scales.

Daubechies formulated the closest to zero-phase filters that minimize this phase shift, which are now widely used in DWT [11]. However, these filters cannot achieve the exact zero phase [12]. Considering this issue, Lenis *et al*. presented a modified version of SWT that addressed the phase-free transformation property [10]. In addition to applying SWT to the signal, the authors reversed the signal and applied SWT to the resulting series. The transformed signal was reversed at each scale and added to the original transformed signal. Coefficients

resulting from this procedure have zero phase shift. As a result of this phase shift elimination, authors claimed the ability to accurately identify the beginning of the P-wave. As another approach, we implemented an SWT-based zero-phase filter bank in our previous study [72]. In this approach, the detail and approximation coefficients were reversed after each level, filtered again, and then reversed one more time to eliminate the phase shift. However, considering the loss of phase information at each scale, this filter bank does not provide the opportunity to reconstruct the signal. Alternatively, Percival presented an elegant solution to the wavelet phase shift issue by introducing a zero-phase wavelet called Zephlet transform [73][74]. In this method, the wavelet filters undergo additional analysis to have their phase equal to zero. Therefore, with the filters not generating any phase shift at each scale, all the resulting coefficients would have zero phase shift with respect to the original signal. Furthermore, this transformation provides perfect reconstruction because Zephlet filters are designed in a way that they satisfy the wavelet filter requirements.

Another benefit of complete synchrony among various Zephlet scales is the opportunity of incorporating information from these scales. As discussed earlier, studies use different details with limited frequency ranges to detect the QRS complexes. However, the frequency range of ECG varies from 0.1 to 100 Hz, which may cover the frequency range of all or several details considering the sampling frequency. Therefore, the advantage of involving more scales could lead to a considerable increase in heartbeat detection performance. This is not possible

for SWT details due to the phase shift that is in the order of tens of milliseconds, while the length of a QRS complex is generally around 100ms.

Non-standard positioned, *e.g.* upper arm electrodes introduce a more challenging requirement to extract ECG-related information due to EMG intensity. Therefore, the synchrony of features' information with respect to ECG plays a critical role in these cases.

With respect to the second SWT drawback, some studies have chosen alternative data-driven methods over SWT, such as EMD or PCA, for ECG delineation to avoid a mother wavelet selection or an optimization problem [47], [67], [75]. Some studies, on the other hand, have investigated the selection of different mother wavelets, such as Haar [76], Daubechies [77], Mexican hat [78], Morelet [79], and Coeiflet [64], [65] for ECG delineation application. ECG signal includes morphological characteristics that play an important role in detecting and identifying CVD conditions diagnoses such as cardiac arrhythmias, myocardial infarctions, atrial enlargements, ventricular hypertrophies, and bundle branch blocks. An accurate classification becomes even more challenging in noisy environments, *e.g.* recordings from non-conventional places over the body surface, a likely scenario for many wearables. Therefore, algorithms that have high robustness against noise and interference are required. The similarity between the QRS complex and the mother wavelet is critical to consider in QRS detection. An optimal mother wavelet will not only produce the highest local maxima of the ECG signal in wavelet components [80], but it can also enhance the PQRST morphology

preservation. Considering the wide range of suggested mother wavelets for ECG delineation in the literature, the selection of an optimal mother wavelet is yet an open issue.

Other methods have also explored ECG signal processing and feature extraction techniques, such as neural networks, mathematical morphology filtering, sparse filtering, Hilbert transform, and matched filters [60].

Although the extracted features play a critical role in localizing the beats by providing the required information, implementing effective algorithms for making a proper decision toward the detection of heartbeats from those features is also a challenge.

2.3.6 Decision Making

After extracting proper features with the aim of enhancing heartbeat detection performance, a decision must be made regarding the occurrence of a heartbeat or QRS complex. There are multiple techniques, with the most conventional and common being the thresholding technique:

$$X_{th} = \beta max\{X[n]\}$$

(2-1)

The threshold is set to a fraction of the maximum amplitude of the feature. The fraction $0 < \beta < 1$ has different values, such as 0.3 [81] and 0.4 [37] used in previous studies. Furthermore, the length of the signal to be processed (e.g., 33 s [82]) has been chosen experimentally.

However, this method does not guarantee a high performance, specifically in noisy environments. Pan and Tompkins introduced Pan-Tompkins [83] as a real-time approach in which the amplitude, slope, and width of the signal are analyzed. Pre-processing is also used to reduce false detections, which makes it a better choice for noisy environments compared to conventional thresholding methods. Firstly, a band-pass filter between 1-15 Hz is applied to the input to suppress muscle noise, baseline wander, power-line interference, and T-wave. The cut-off frequencies are selected based on the QRS-complex dominant frequency range. Secondly, signal differentiation is applied using a five-point derivative to provide the QRS-complex slope information. Next, the resulting signal is squared point-by-point to make the QRS complex more pronounced by emphasizing the higher frequencies. Lastly, moving window integration (150 ms) is applied to obtain waveform information along with the QRS-complex slope. The output is then used to detect the heartbeats (R-peaks) using an adaptive thresholding technique.

Zero-crossing [84], neural network [85], singularity analysis [47], and matched filters [86] have also been applied to increase detection accuracy.

Chapter 3

Heartbeat detection from single-lead ECG contaminated with simulated EMG at different intensity levels: a Comparative Study

The contents provided in this chapter are parts of a journal manuscript that has been accepted to be published in the Biomedical Signal Processing and Control journal. N. Heydari Beni and N. Jiang, "Heartbeat detection from a single-lead ECG contaminated with simulated EMG at different intensity levels: a comparative study," *Biomed. Signal Process. Control*, Jan. 2023.

3.1 Introduction

In this study, we implemented five state-of-the-art pipelines and investigated their performance in heartbeat detection at four different noise levels. We generated these various noise levels by adding simulated EMG to ECG signals. These implemented algorithms were expected to perform differently in an environment with a specific noise level. Furthermore, their performance was expected to decrease when the noise level increased. But the amount of change could be different among these five pipelines. We considered two directions in the selection of a pipeline that works the best in heartbeat detection. The first direction was to compare all five at each noise level and select the best-performing pipeline per noise level. This way, we will have the chance to alter the detection algorithm as the noise level changes for a future

application. The next direction was to investigate the pipelines' robustness against noise and select one that has the most robustness. Accordingly, we will have the option of choosing one particular pipeline to use for an environment with changing noise levels.

In the next section, the dataset and methodologies used in this study are described in detail. In Section 3, the comparison of all the implemented pipelines' performance at different contamination levels is presented. Section 4 discusses the results, and the conclusion and directions for future work are provided in Section 5.

3.2 Methodology

3.2.1 Dataset Description

3.2.1.1 Dataset 1

In the current study, the data from the MIT-BIH Arrhythmia Database was used as Dataset 1 [87]. The database consists of ECG recordings from 47 subjects studied by Beth Israel Hospital (BIH) Arrhythmia Laboratory between 1975 and 1979. All recordings in the database were sampled by 360 Hz. Two or more cardiologists independently annotated each record, and the resulting annotations are also included in the database. In the current study, the data from lead MLII (Modified Lead II) for 20 subjects (male: nine, female:11) with ages between 24 and 87 were selected from the database. We only focused on normal heartbeats in this study. Therefore, there was a need to find consecutive heartbeats annotated as normal

31

among all the participants' data. This constraint reduced the number of subjects to 20 and the length of the signal to 28 sec, to be shared among all the subjects.

3.2.1.2 Dataset 2

We used Lead II from a dataset recorded in an experimental setup at our laboratory as Dataset 2 for this study. Twenty participants with no known cardiac, circulatory system, blood, or lung problems or allergy to adhesive or rubbing alcohol were recruited for the experiment. The protocol was approved by the Office of Research Ethics of the University of Waterloo (ORE #41252), considering all the Covid-19 safety requirements. Prior to the start of the experiment, each participant signed a Written Informed Consent. The participants were seated in a chair and relaxed. Two standard EMG electrodes were attached to the participants on the right arm and left leg to record Lead II. The commercial EMG device recorded the signals from all the electrodes. Data were recorded using the EMG-USB2+ biosignal amplifier, with a hardware band-pass filter from 0.3 Hz to 500 Hz. The recordings were digitized with a sampling frequency of 2048 samples/second. The generally acceptable frequency range of diagnostic ECG is from 0.05 to 100 Hz [23]. Therefore, the data was lowpass-filtered using a third-degree Butterworth filter with a cut-off frequency of 100 Hz. Furthermore, data were downsampled with the rate of eight to change the sampling frequency to 256 Hz. Five minutes of rest session was recorded from each participant, from which the first 28 seconds were used in this study to be consistent with Dataset 1Dataset 1.

3.2.2 Simulation of EMG Contamination

EMG signals, when overlaid with ECG, can considerably affect the performance of algorithms for heartbeat detection from ECG. Therefore, the robustness of the heartbeat detection algorithms with the presence of different levels of EMG artifact should be investigated. In the current study, four levels of simulated artifacts were generated and added to the ECG signals in the dataset to simulate various muscular activity levels, as shown in the left panel of Figure 3-1. Gaussian random noise [88]–[90] was generated first, and then anti-aliasing filtering was applied. The cut-off frequency was selected as 100 Hz considering the description of both datasets. The high-pass filter was applied with the cut-off frequency of 6 Hz to convert the white noise to a coloured noise considering the frequency content of EMG
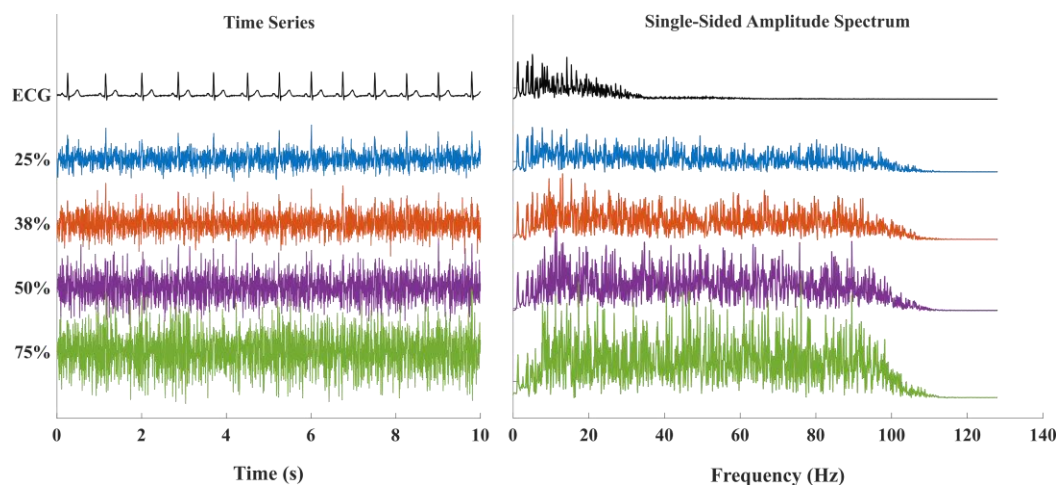
Figure 3-1. The ECG contamination representation in time (left panel) and it's power spectrum (right panel). The simulated EMG with variable STD (25%, 35%, 50%, 75% of the range of ECG: rows 2-5) was added to the ECG signal (first row, left panel). The frequency content of each signal can be found in the right panel right in front of the respective signal.

(see Figure 3-1, right panel). Moreover, the level of muscle contraction was controlled by the Standard Deviation (STD) of the coloured noise. The STD was set to a fraction (0.25, 0.38, 0.5, 0.75) of the ECG signal's range for noise levels one (N_1) to noise level four (N_4). We calculated SNR for these contaminated ECG signals as follows:

$$\text{SNR} = 20 \times \log \frac{\text{Max (ECG) - Min (ECG)}}{3 \times \text{STD (coloured noise)}} \tag{3-1}$$

The SNR for N_1 to N_4 equals 2.4 dB, -1.18 dB, -3.8 dB, and -7 dB, respectively.

3.2.3 Feature Extraction

We investigated five pipelines with different feature extraction approaches to detect the heartbeats from the contaminated ECG signal for each dataset. The schematic diagram of these pipelines is illustrated in Figure 3-2 and described in detail as follows.

3.2.3.1 CEEMDAN

Huang et al. introduced EMD as an adaptive and fully data-driven technique that decomposes the signal under analysis into oscillatory components or modes (IMFs). In EMD,
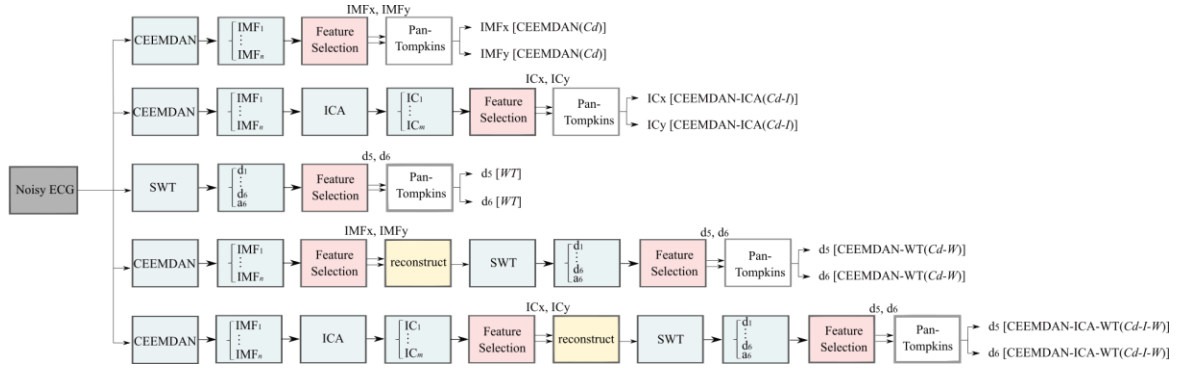
Figure 3-2. The schematic diagram of the implemented methods. Five different pipelines were applied to extract features from contaminated ECG. Some of the features were manually selected for heartbeat detection. Pan-Tompkins was then applied to the extracted features as the heartbeat detection step. The pipelines are CEEMDAN (*Cd*), CEEMDAN-ICA (*Cd-I*), *WT*, CEEMDAN-WT (*Cd-W*), and CEEMDAN-ICA-WT (*Cd-I-W*) in the order of rows.

there is no need to set a priori the level of decomposition. In an iterative procedure called the

sifting process, EMD decomposes signal into a variable number of components:

$$x(t) = \sum_{k=1}^{I} \text{IMF}_k(t) + r_N(t) \tag{3-2}$$

where x is the signal to be decomposed, I is the number of iterations and r_N is the residual. The

extracted IMFs are dynamic and consist of different frequency components. Therefore, each

IMF can be rejected or retained to partially reconstruct the signal based on the desired

application. Because IMFs are additive, linear filtering or other linear transformation methods

such as ICA can also be performed on the IMFs. However, when the signal and noise amplitudes

and frequencies are not sufficiently different, mode-mixing will occur, resulting in single-tone

amplitude-modulated IMFs [55]. To overcome this issue, the EEMD has been presented. In this method, a number of white noise series, $n_i(t)$, are generated and added to the signal separately:

$$x_i(t) = x(t) + \epsilon_0 n_i(t) \tag{3-3}$$

where $x_i(t)$ is the ith ($i=1\ldots, I$) noisy version of the signal, $n_i(t)$ is a zero-mean, unit-variance white noise ($N(0,1)$), and ϵ_0 is the STD of the added noise. The normal EMD procedure is then applied to each of the noisy versions, $x_i(t)$, resulting in a set of IMFs. Therefore, I different IMFs, $IMF_k^i(t)$, ($i=1, \ldots, I$), for the kth empirical mode will be generated. The final IMF for the kth mode, namely $IMF_k(t)$, is the ensemble average of the $IMF_k^i(t)$:

$$IMF_k(t) = \frac{1}{I} \sum_{i=1}^{I} IMF_k^i(t) \tag{3-4}$$

EEMD suffers from some limitations, such as having some noise residue in the extracted IMFs and a different number of modes at different realizations. Therefore, CEEMDAN has been presented to overcome these issues. For the sake of simplicity, CEEMDAN will be referred to as Cd hereinafter. The details of Cd is presented in [7]. It is described briefly below for the sake of clarity:

1. I noisy versions of the original signal are generated as $x_i(t) = x(t) + \epsilon_0 n_i(t)$, the same of in EEMD;

2. When $k=1$, $IMF_1(t)$ is obtained as in EEMD:

36

$$E_1(x_i(t)) = \text{IMF}_1^i(t) \qquad\qquad (3\text{-}5)$$

$$\text{IMF}_1(t) = \frac{1}{I} \sum_{i=1}^{I} \text{IMF}_1^i(t) \qquad\qquad (3\text{-}6)$$

where $E_k(.)$ is the empirical mode operation that produces the kth mode obtained by EMD.

3. $\text{IMF}_1(t)$ is subtracted from the original signal to obtain the first residue: $r_1(t) = x(t) - \text{IMF}_1(t)$

4. The second Cd mode $\text{IMF}_2(t)$ is:

$$\text{IMF}_2(t) = \frac{1}{I} \sum_{i=1}^{I} E_1(r_1(t) + \epsilon_1 E_1(n_i(t))) \qquad\qquad (3\text{-}7)$$

And the second residue, $r_2(t)$, will then calculates as:

$$r_2(t) = r_1(t) - \text{IMF}_2(t) \qquad\qquad (3\text{-}8)$$

5. For $k = 2, ...,$ the kth residue is calculated as $r_k(t) = r_{k-1}(t) - \text{IMF}_k(t)$, and the $(k+1)$th mode is:

$$\text{IMF}_{k+1}(t) = \frac{1}{I} \sum_{i=1}^{I} E_1(r_k(t) + \epsilon_k E_k(n_i(t))) \qquad\qquad (3\text{-}9)$$

6. The iterative process repeats until the obtained residue is a monotone function, and the final residue is:

$$R(\text{t}) = x(\text{t}) - \sum_{k=1}^{K} \text{IMF}_k(\text{t}) \qquad (3\text{-}10)$$

7. And the signal $x(t)$ can be reconstructed as:

$$x(t) = R(t) + \sum_{k=1}^{K} \text{IMF}_k(t) \qquad (3\text{-}11)$$

where K is the final number of modes.

Considering the sampling frequency of the ECG signal is 360 Hz and 256 Hz in Datasets 1 and 2, respectively, IMFs include frequency ranges of 0-180 Hz for Dataset 1 and 0-128 Hz for Dataset 2. The highest frequency content in both datasets belongs to the added simulated EMG with the frequency range of 6-100 Hz. Therefore, it is expected for the initial IMF(s) to contain EMG-related information and for QRS complex-related information to be captured in the higher order IMFs. In Figure 3-3, an example of ECG from Dataset 2, contaminated ECG, and IMFs (left panel) and their respective frequency spectrum (right panel) can be seen. As shown in Red colour, IMF_4 and IMF_5 were manually selected because they had the most similarity to ECG signal and the most overlap with the frequency content of QRS complexes (with the dominant frequency range of ~10-21 Hz). In another example in Figure 3-4 (see left

38

panel), you can see the selected IMFs are IMF_3 and IMF_4 with the most similarity to the ECG signal. In both of these examples, the initial IMFs mostly contained EMG-related information, and QRS complexes were captured in the higher-order IMFs.
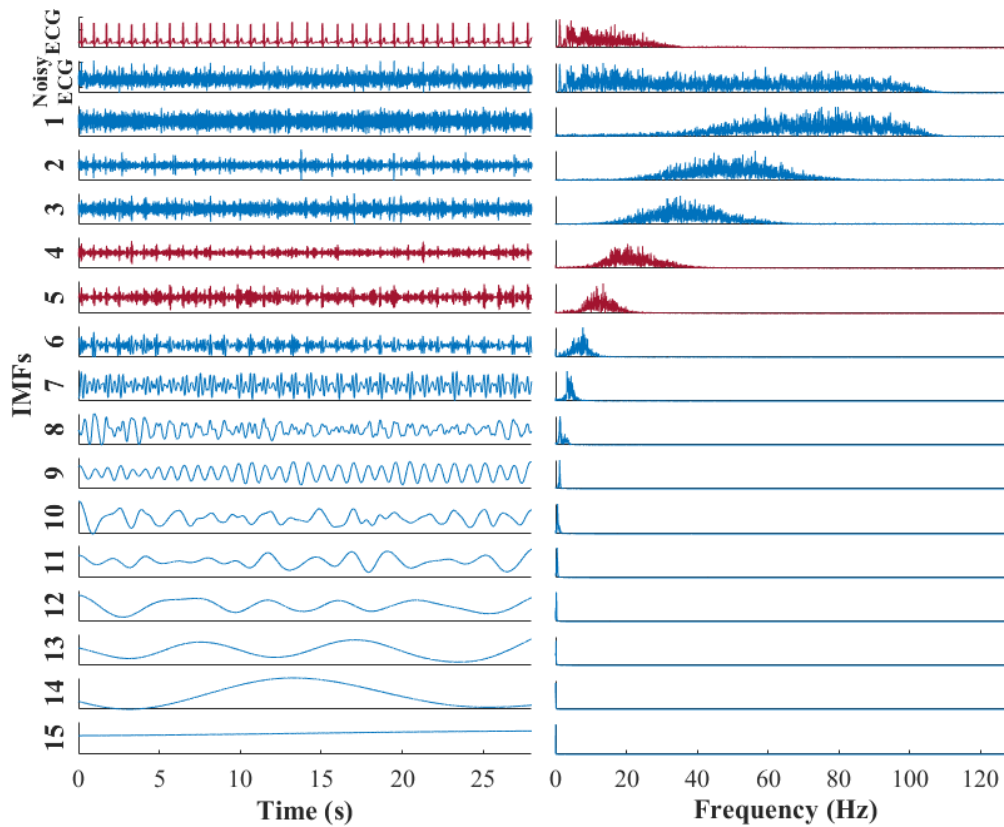
Figure 3-3 An example of the extracted components from applying CEEMDAN (left panel) and their respective frequency spectrum (right panel). Among the extracted IMFs, the red signals, IMF_4 and IMF_5, were selected manually because of their higher similarity to ECG. The frequency spectrum of the selected IMFs also has the most overlap with ECG signal. As shown, the first IMFs have higher frequency content overlap with contaminated ECG (or simulated EMG signals).
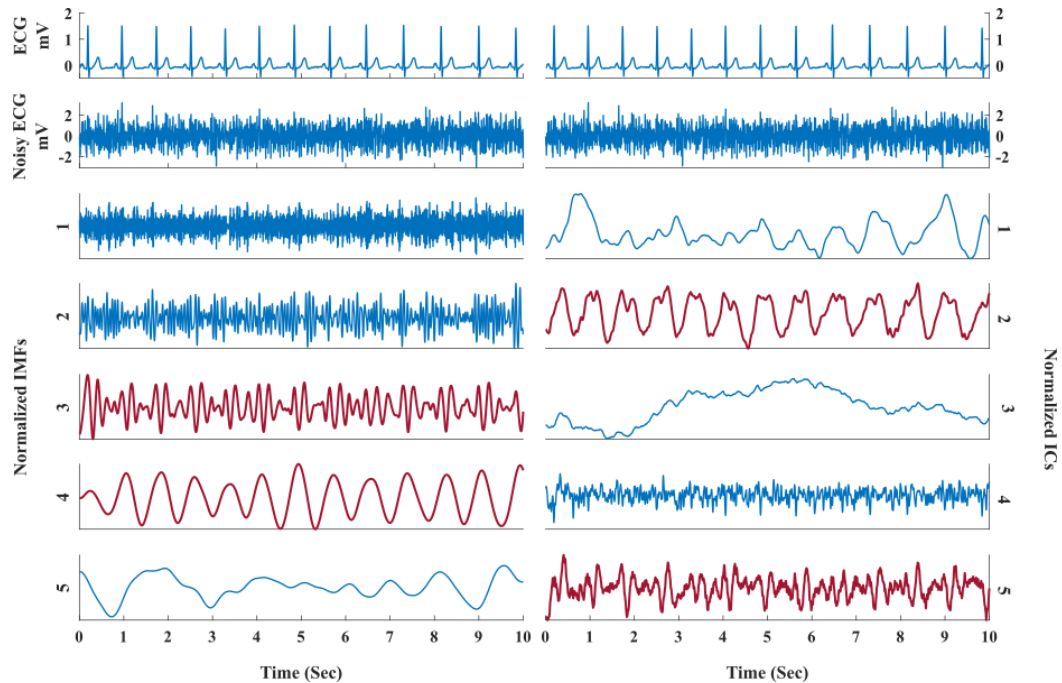
Figure 3-4. Some examples of the extracted components from applying *Cd* (left panel) *and Cd-I* (right panel) to contaminated ECG. Left: Among the extracted IMFs, the bold red signals, IMF$_x$ and IMF$_y$, were selected manually because of their higher similarity to ECG. Right: Resulting ICs after applying fast-ICA to the extracted IMFs achieved from *Cd* are shown. The bold red signals are the manually selected components, *i.e.* IC$_x$ and IC$_y$ which had the highest similarity to ECG.

In the first pipeline, as shown in Figure 3-2, we used CEEMDAN for feature extraction and then selected the two IMFs in the feature selection phase. Then, we applied a heartbeat detection algorithm on the selected features separately, which will be explained in detail. For the sake of simplicity, this pipeline will be referred to as *Cd* hereinafter.

40

3.2.3.2 CEEMDAN-ICA

The extracted IMFs using *Cd* still contain both EMG- and ECG-related content. Because it is reasonable to assume the statistical independence between EMG and ECG, ICA (fastICA [91]) has been used to separate the two. In this pipeline, fast-ICA was applied to the IMFs obtained by *Cd* to further improve signal quality (the second row of Figure 3-2). Two of the resulting independent components were manually chosen for heartbeat detection (see the right panel of Figure 3-4). These selected features, *i.e.* IC_x, IC_y, shown in the second row from the top of Figure 3-2, were selected for subsequent heartbeat detection processing. This pipeline will be called as *Cd-I* hereinafter for simplicity.

3.2.3.3 SWT, CEEMDAN-SWT, and CEEMDAN-ICA-SWT

Considering the frequency range of EMG between 6 and 500 Hz with the most power between 20 and 150 Hz [33], compared to that of ECG mainly under 21 Hz, filtering out some noninterest frequency components will help with achieving a cleaner ECG signal. For this matter, we applied SWT at the level of six to the signal. SWT coefficients of detail components one to six correspond to frequency ranges of 90-180 Hz, 45-90 Hz, 22.5-45 Hz, 11.25-22.5 Hz, 5.75-11.25 Hz, 2.875-5.75 Hz, respectively, and 0-2.875 Hz for the approximation component for Dataset 1. These frequency ranges change to 64-128 Hz, 32-64 Hz, 16-32 Hz, 8-16 Hz, 4-8 Hz, and 2-4 Hz, respectively, for detail components one to six and 0-2 Hz for the approximation component for Dataset 2. The frequency range of QRS complexes is under

41

~21Hz, which has considerable overlap with EMG frequency content starting from 6 Hz. Therefore, to simultaneously reject components dominated by EMG and retain with QRS-complex, d_5 and d_6 with the frequency content between 2.875-11.25 Hz for Dataset 1 and 2-8 Hz for Dataset 2 were chosen in the *WT* pipeline (the third row from the top in Figure 3-2).

In addition to applying SWT to the contaminated ECG signal described in this Section, we also applied SWT to the reconstructed signal obtained from the selected features in the first two pipelines, i.e. *Cd* and *Cd-I*, which yielded CEEMDAN-WT (*Cd-W*) and CEEMDAN-ICA-WT (*Cd-I-W*). In the *Cd-W* pipeline, we calculated the reconstructed version from the Cd pipeline by summing up the two selected IMFs (IMF_x and IMF_y). In the *Cd-I-W* pipeline, we projected the preserved ICs from the IC space back to the IMF space. The Summation of these IMFs provided a reconstructed version of contaminated ECG. Details and approximation selection was identical to those in the *WT* pipeline earlier by choosing d_5 and d_6.

3.2.4 Heartbeat Detection

We used a modified version of Pan-Tompkins [83] for heartbeat detection from each selected feature. Pan-Tompkins includes a pre-processing phase, as described in the following steps. With minor changes, we first applied a band-pass filter between 1-15 Hz to the input to suppress muscle noise, baseline wander, 60 Hz interference, and T-wave. The cut-off frequencies were selected based on the QRS-complex dominant frequency range. Secondly, we applied signal differentiation using a five-point derivative to provide the QRS-complex

42

slope information. Next, we squared the resulting signal point-by-point to make the QRS complex more pronounced by emphasizing the higher frequencies. Lastly, we applied moving window integration (150 ms) to obtain waveform information along with the QRS-complex slope. We then used the output to detect the heartbeats (R-peaks) using an adaptive thresholding technique. We made some main changes to the original Pan-Tompkins in consideration of the substantially higher noise levels in the current study compared to the original Pan-Tompkins paper. First, we considered a fixed minimum (200 ms) and maximum distance between the beats. We chose the maximum distance of 1300 ms and 1100 ms for lower and higher heart rates, respectively. We manually determined the threshold for lower/higher heart rates to be 57 beats per minute. Second, instead of applying heartbeat detection on both the raw and pre-processed signals, we only used the pre-processed signal for the detection because the raw signal was too noisy to consider. Third, in the original Pan-Tompkins method, there is a step that considers the detected heartbeats with a shorter than 360ms distance from the previously detected heartbeat as a T-wave and ignores them. However, we did not implement this step in this study to reduce the possibility of losing a potential heartbeat in a noisy environment.

3.2.5 Performance Metrics and Statistical Analysis

In order to evaluate the performance of the Pan-Tompkins detection algorithm on the investigated features, we calculated sensitivity (*SE*), positive predictive value (*PPV)* and the F_1 score.

$$\text{Sensitivity } (SE) = \frac{TP}{TP+FN} \tag{3-12}$$

$$\text{Positive Predictive Value } (PPV) = \frac{TP}{TP+FP} \tag{3-13}$$

$$F_1 = \frac{2 \times PPV \times SE}{PPV+SE} \tag{3-14}$$

where *TP* or true positive refers to the number of beats that were detected within less than 150 ms of distance from a heartbeat. The *FN* or false negative is the number of heartbeats that were not detected, and lastly, *FP* stands for the number of beats that were mistakenly detected. *SE* measures how well an algorithm can detect heartbeats and *PPV* represents how precise the detection is. F_1 is also a measure of accuracy, which is used to compare the algorithms considering both the *SE* and *PPV*.

The heartbeat detection using the selected features in each pipeline was repeated five times with different series of coloured noise from N_1 to N_4 for both datasets. Therefore, considering the 20 subjects, there were 100 outputs for both *SE* and *PPV* for each feature at each noise level. A mixed-model Analysis of Variance (ANOVA) was used to compare the algorithms. The

multiple comparison test, post hoc Bonferroni, was used to adjust the significance level for the fact that multiple comparisons needed to be made. At each noise level, the feature with the higher F_1 was selected from all the pipelines. Furthermore, the selected features from the pipelines were compared using the post hoc Bonferroni multiple comparison test to find the best feature at each noise level.

3.3 Results

An example of detected heartbeats using *Cd*, *WT*, and *Cd-I* pipelines from a contaminated heartbeat selected from Dataset 2 with simulated EMG at the four intensity levels is shown in Figure 3-5. IMFx from *Cd*, d_6 from *WT* and ICx from *Cd-I* were used in this example. As shown, there is a time difference between the detected and real heartbeats, which in this example varies from 30 ms to 60 ms.

3.3.1 Feature selection for each pipeline

The *SE* and *PPV* for all the investigated pipelines averaged on 20 subjects, and five trials are shown in the top panel of Figure 3-6 and Figure 3-7, respectively, for Dataset 1 and Dataset 2. From the figures, it is evident that different pipelines and features resulted in different patterns of performance trajectory as the noise level increased.

From Dataset 1, in the *Cd* and *Cd-I* pipelines, there was a reduction in both *SE* and *PPV* across noise levels with both features. However, IMF_y from *Cd* and IC_x from *Cd-I* pipelines performed consistently and significantly ($p < 0.05$) better than IMF_x and IC_y, respectively. For
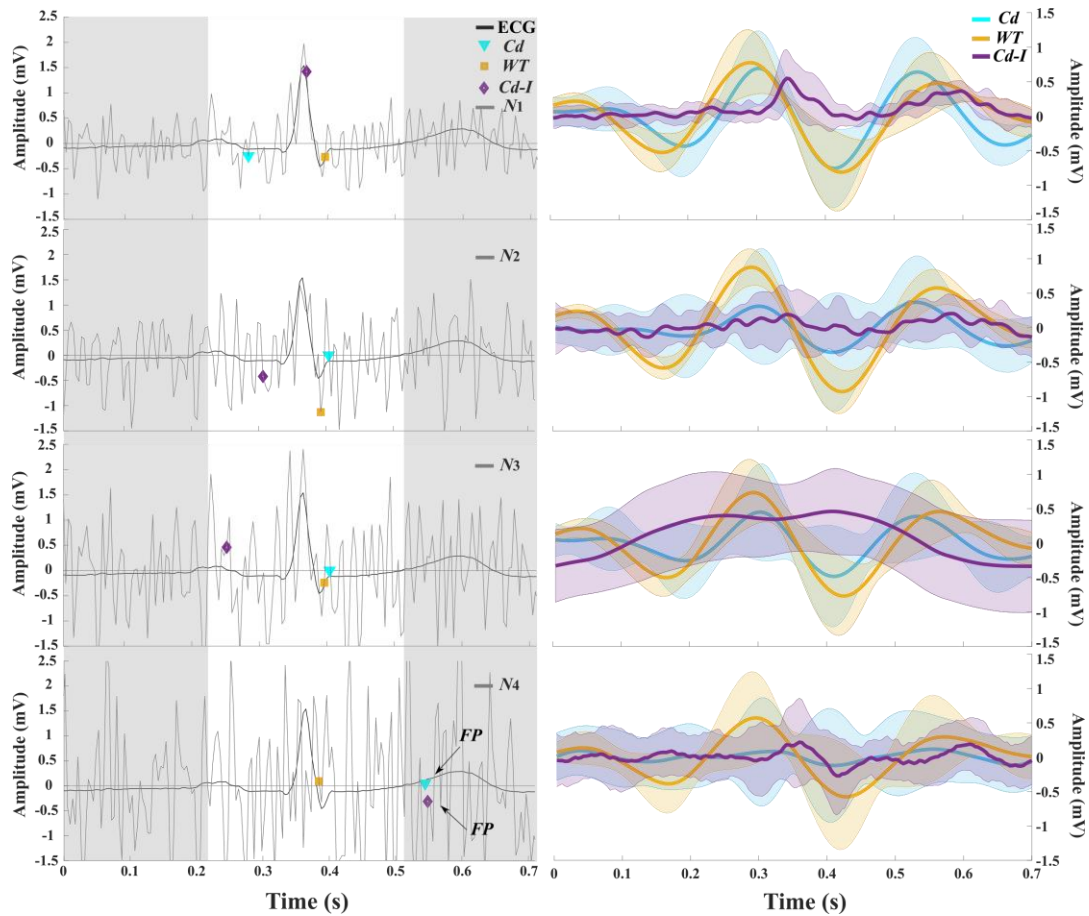
Figure 3-5. An example of a heartbeat contaminated with four levels of EMG intensity along with the detected heartbeat locations from *Cd*, *WT*, and *Cd-I* pipelines (left) and the averaged normalized heartbeat over an average of 38 detected heartbeats (right). The shaded area around each averaged normalized heartbeat in the right panel represents the STD. The white rectangle at the left panel shows the acceptable distance between the detected and the real heartbeat. As expected, detected locations outside of this range are considered as *FP* as illustrated in the left panel.
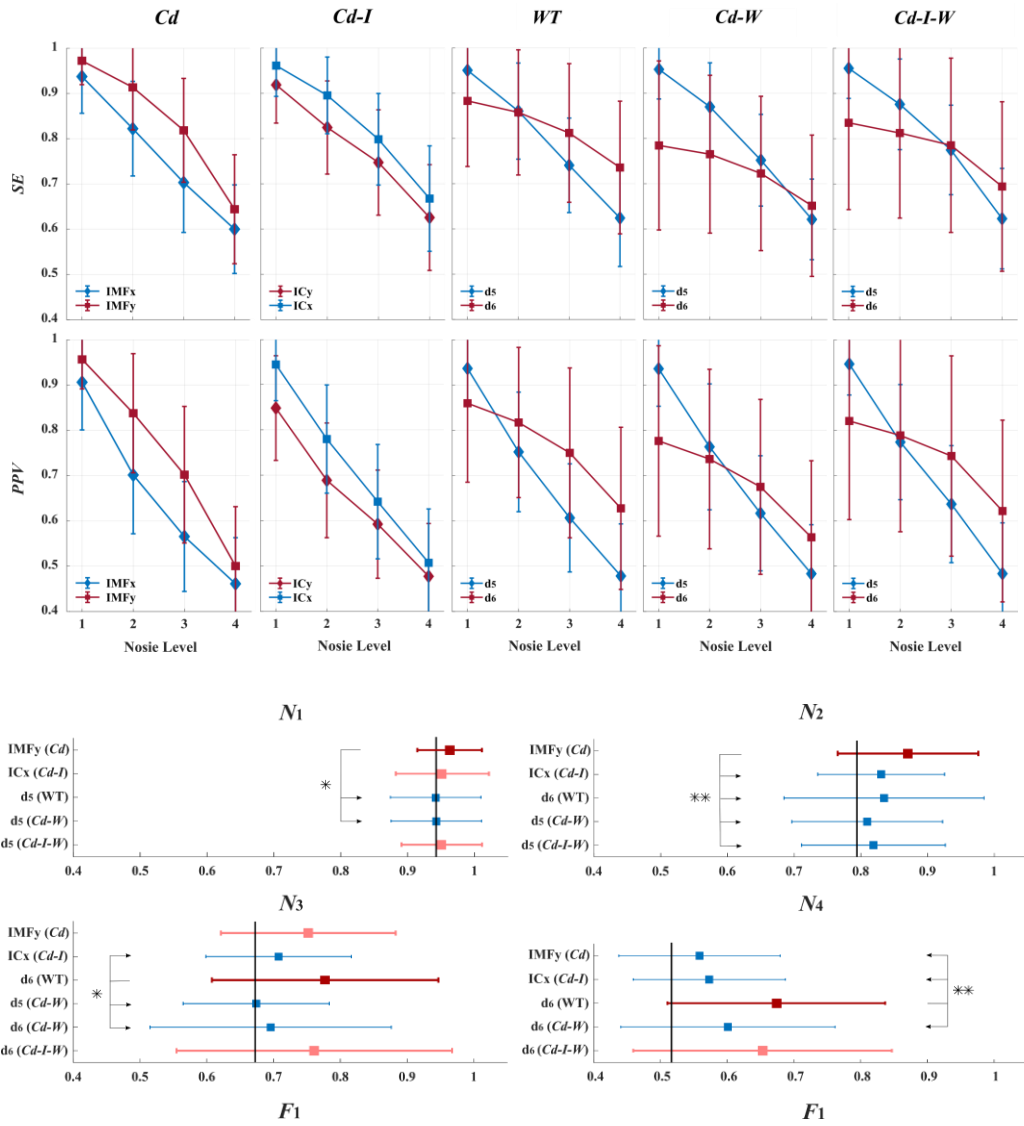
Figure 3-6. First and second rows: The performance of different pipelines in terms of *SE* and *PPV* at various noise levels averaged on 20 subjects and five trials from Dataset 1. Third and fourth rows: The highest results from all pipelines at each noise level: N_1: top left, N_2: top right, N_3: bottom left, N_4: bottom right. The red lines indicate the highest F_1 at each noise level. The pink lines represent the not statistically different F_1 compared to the red lines, and the blue lines represent significantly lower F_1s ($p<0.01$, *$p<0.05$). As expected, by increasing noise level, the highest F_1 decreased.**

WT, *Cd-W*, and *Cd-I-W*, d_5 provided a superior performance compared to d_6 at N_1 ($p < 0.01$),
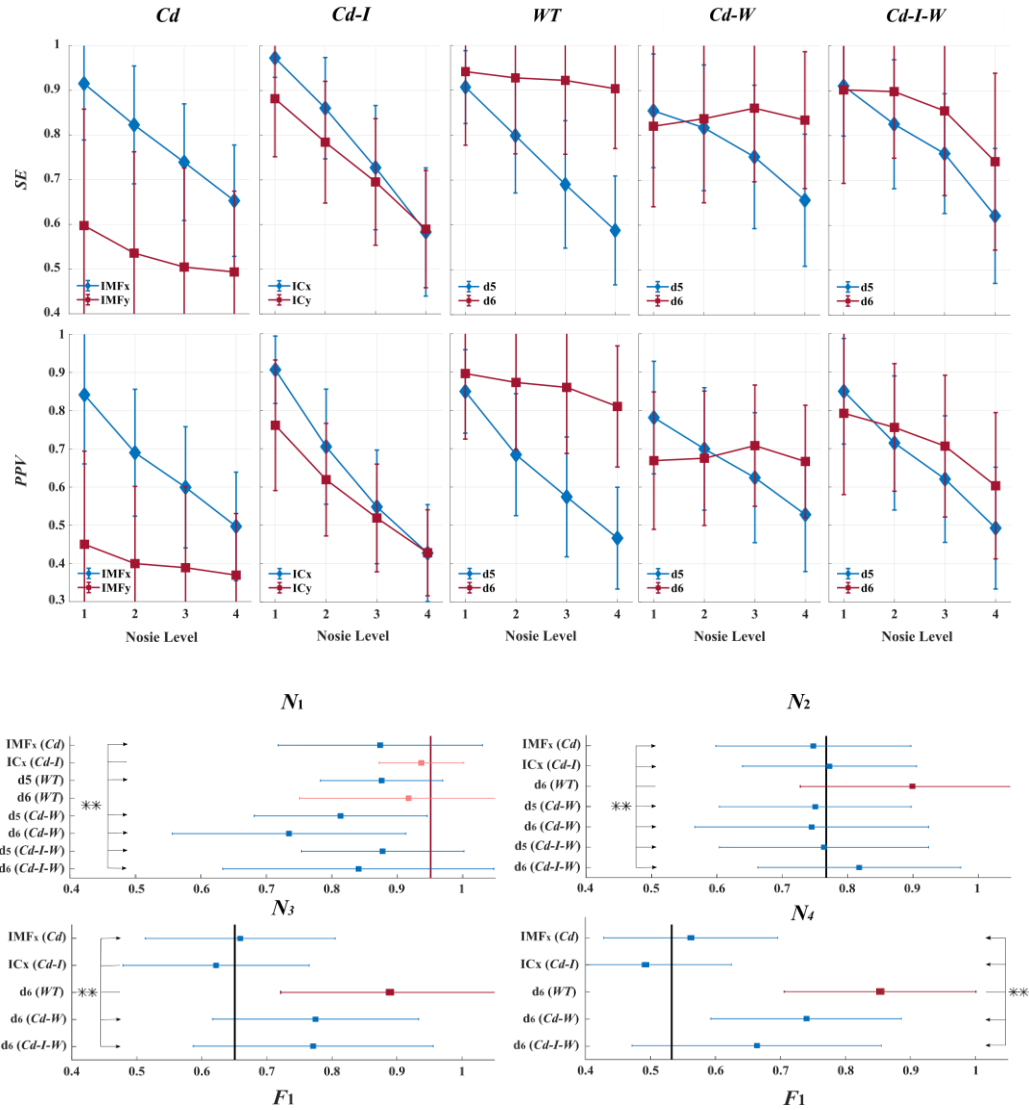
Figure 3-7. First and second rows: The performance of different pipelines in terms of *SE* and *PPV* at various noise levels averaged on 20 subjects and five trials from Dataset 2. Third and fourth rows: The highest results from all pipelines at each noise level: N_1: top left, N_2: top right, N_3: bottom left, N_4: bottom right. The red lines indicate the highest F_1 at each noise level. The pink lines represent the not statistically different F_1 compared to the red lines, and the blue lines represent significantly lower F_1s (** $p<0.01$). As expected, by increasing noise level, the highest F_1 decreased.

however, it encountered a larger reduction in the performance trajectory from N_1 to N_4.

Consequently, d_6 attained a significantly better performance at N_4 ($p < 0.01$) in both *SE* and *PPV* terms.

From dataset 2, IMF_x from *Cd* pipeline performed consistently and significantly better than IMF_y ($p < 0.01$). IC_x from *Cd-I* pipeline provided a better performance ($p < 0.01$) at N_1 and N_2. However, IC_y gained the same performance as IC_x at N_3 and N_4 ($p > 0.05$) in terms of both *SE* and *PPV*. For *WT*, d_6 performed consistently better than d_5 ($p < 0.01$) at noise levels N_2-N_4. For N_1, d_6 performed significantly better than d_5 in terms of *PPV* ($p < 0.05$) but the same in terms of *SE* ($p > 0.05$). For *Cd-W*, d_5 provided a better performance compared to d_6 in terms of *SE* and *PPV* at N_1 ($p < 0.01$). At N_2, they had the same performance ($p > 0.05$), and then d_6 obtained a higher performance at N_3 and N_4 ($p < 0.01$). For *Cd-I-W*, d_5 provided a superior performance than d_6 ($p < 0.01$) at N_1 in terms of *PPV* yet the same performance in terms of *SE* ($p > 0.05$). At N_2, d_6 gains superior *SE* ($p < 0.01$) and the same *PPV* ($p > 0.05$) compared to d_5. At N_3 and N_4, d_6 performed significantly better than d_5 in terms of both *SE* and *PPV*.

3.3.2 Feature selection for each noise level

Considering both *SE* and *PPV*, the results for selected features in terms of F_1 at each noise level are illustrated in the lower panel of Figure 3-6 and Figure 3-7 for Dataset 1 and Dataset 2, respectively. These results provide a balanced assessment of the best-performing feature of the pipelines at different noise levels.

3.3.2.1 Dataset 1

The highest F_1 scores are shown with a red line at each noise level, as illustrated in the second panel of Figure 3-6. The vertical lines represent the F_1 score of Pan-Tompkins on the noisy signal without applying any feature extraction methods prior, which we call Baseline (BL) hereinafter. At N_1, the F_1 scores of IMF_y (*Cd*), IC_x (*Cd-I*), and d_5 (*Cd-I-W*) were 0.96 ± 0.05, 0.95 ± 0.07, and 0.95 ± 0.06, respectively. And post hoc Bonferroni test found no significant difference among them ($p > 0.05$). But they were significantly higher than the other pipelines ($p < 0.05$). Among these pipelines, IMF_y (*Cd*) was significantly better than BL ($p < 0.05$). At N_2, the F_1 score of IMF_y (*Cd*) was 0.87 ± 0.11 and significantly higher than BL and the other pipelines ($p < 0.01$). At N_3, the F_1 score of d_6 (*WT*), d_6 (*Cd-I-W*), and IMF_y (*Cd*) were 0.78 ± 0.17, 0.76 ± 0.21, and 0.76 ± 0.21. The post hoc Bonfferoni test found no significant difference among them ($p > 0.05$). But they were significantly higher than BL and the other features ($p < 0.05$). At N_4, the F_1 score of d_6 (*WT*) and d_6 (*Cd-I-W*) were 0.67 ± 0.16 and 0.65 ± 0.19 and not significantly different from each other ($p > 0.05$). But they were significantly higher than BL and the features from the other features ($p < 0.01$).

Taken together, these results suggest that in less noisy environments (*i.e.* N_1 and N_2), IMF_y (*Cd*) provides more accurate heartbeat detection for Dataset 1. However, d_6 (*WT*) and d_6 (*Cd-I-W*) held a higher performance among the other features in environments with higher levels of noise (*i.e.* N_3 and N_4).

3.3.2.2 Dataset 2

The highest F_1 scores are shown with a red line at each noise level for Dataset 2, as illustrated in the second panel of Figure 3-7. The vertical lines represent the F_1 score of BL. At N_1, the F_1 scores of IC_x (*Cd-I*) was the same as BL (0.94 ± 0.06 vs. 0.95 ± 0.05; $p > 0.05$) and d_6 (*WT*) (0.92 ± 0.16; $p > 0.05$) but significantly higher than the other features ($p < 0.01$). At N_2, the F_1 score of d_6 (*WT*) was 0.90 ± 0.17 and significantly higher than BL and the other features ($p < 0.01$). Furthermore, d_6 (*WT*) maintained its superiority at N_3 and N_4 with the F_1 score of 0.89 ± 0.15 and 0.85 ± 0.16, respectively. The post hoc Bonferroni test found its performance to be significantly better than BL and the other features ($p < 0.01$) at both N_3 and N_4 as illustrated in the second panel of Figure 3-7.

These results suggest that d_6 (*WT*) provides a more accurate heartbeat detection for Dataset 2 at N_2- N_4. At N_1, IC_x (*Cd-I*) provides the highest accuracy, yet not significantly better than d_6 (*WT*), which makes *WT* pipeline the best choice for all the noise levels.

3.3.3 Robustness to increasing noise levels

The level of performance degradation with increasing noise levels represents the robustness against the noise of a processing pipeline. For Dataset 1, the reduction of *SE* from N_1 to N_4 was 34% and 31% for IMF_y (*Cd*) and IC_x (*Cd-I*), respectively. Moreover, d_5 (*WT*), d_5 (*Cd-W*), and d_5 (*Cd-I-W*) suffered a reduction of 34%, 35%, and 35%. Meanwhile, d_6 (*WT*), d_6 (*Cd-W*), and d_6 (*Cd-I-W*) only lost 17% of *SE* from N_1 to N_4. Therefore, the *SE* reduction of d_6

from pipelines including SWT is considerably lower than the other pipelines. On the other hand, there was a more pronounced effect on *PPV* than *SE* with an increasing level of noise. It reduced 48% and 46% for IMF_y (*Cd*) and IC_x (*Cd-I*), respectively. From the pipelines including SWT, d_5(*WT*), d_5 (*Cd-W*), and d_5 (*Cd-I-W*) suffered a reduction of 49%, 48%, and 50%, respectively. However, d_6 (*WT*), d_6 (*Cd-W*), and d_6 (*Cd-I-W*) lost 27%, 27%, and 24% across noise levels.

For Dataset 2, the reduction of *SE* from N_1 to N_4 was 37% and 43% for IMF_x (*Cd*) and IC_x (*Cd-I*), respectively. Meanwhile, d_6 (*WT*), d_6 (*Cd-W*), and d_6 (*Cd-I-W*) only lost 6%, 6%, and 16% of *SE* from N_1 to N_4. Therefore, consistent with Dataset 1, the *SE* reduction of d_6 from pipelines including SWT is considerably lower than the other pipelines. Furthermore, along with the results from Dataset 1, *PPV* suffered a more pronounced reduction with an increasing level of noise compared to *SE*. It reduced 44% and 52% for IMF_x (*Cd*) and IC_x (*Cd-I*), respectively. From the pipelines, including SWT, d_6 (*WT*), d_6 (*Cd-W*), and d_6 (*Cd-I-W*) lost 10%, 10%, and 20%, respectively, across noise levels.

Along with the results from Dataset 1, we can emphasize the considerably positive effect of SWT utilization in increasing the robustness against noise. This helps explain the superiority of d_6 (*WT*) in the higher noisy environments compared to the other pipelines in both datasets.

3.4 Discussions

ECG-based heartbeat detection algorithms are sensitive to SNR, and their performance will deteriorate in noisy conditions. In an environment with a particular noise level, algorithms perform differently and when this noise level changes, they provide different robustness against noise. Currently, there are few studies in the literature focusing on the analysis of various ECG-based heartbeat detection algorithms under various noise levels, particularly in low SNR scenarios.

We designed the present study to investigate the effect of different levels of EMG artifact on popular ECG-based feature extraction algorithms for heartbeat detection. We implemented five processing pipelines composed of state-of-the-art artifact removal methods for ECG and investigated them at four different SNR levels. We generated these different SNR levels by adding simulated EMG artifacts to ECG signals. The first objective of the study was to identify which method performs the best at each level of EMG artifact contamination. By comparing the performance of different methods at each contamination level, we could identify the best algorithm to use at that particular noise level. Therefore, we can later adjust our detection algorithm in an environment with varying noise levels for future applications. However, we might want to rather use a single algorithm in an environment with varying noise level. A method might perform very well in less noisy environments but get heavily affected when the noise level increases. Accordingly, we investigated the robustness of methods to artifact

increment to select a single algorithm for all noise levels. Hence, the second objective of this study sought to determine which method performs more consistently in the presence of various EMG levels.

With respect to the first objective, *Cd* was identified as the best pipeline to detect heartbeats from less noisy environments (N_1, N_2) for Dataset 1. This finding is consistent with studies that have previously identified CEEMDAN as an effective algorithm for heartbeat detection from clean ECG signals. To name a few, Queyam et al. [92] and Hussain et al. [93] have achieved a *SE* of 98.13% and 99.96% for heartbeat detection using CEEMDAN. Escalona et al. also used EEMD in a wearable long-term heart rhythm monitoring system [10] to increase the SNR of the recorded signal. For Dataset 2, *Cd-I* provided the highest performance in the least noisy environment (N_1). In noisier environments, *WT* and *Cd-I-W* pipelines from Dataset 1 (N_3, N_4) and *WT* pipeline from Dataset 2 ($N_{2,...,} N_4$) provided significantly higher performance. It suggests that *WT* has consistent behaviour across datasets. In terms of computational cost, although CEEMDAN has a considerably reduced computational load compared to EEMD [45], its cost is still higher than SWT. Moreover, the combination of CEEMDAN with ICA in the *Cd-I* pipeline adds more computational overlead. Therefore, *WT* is more consistent (across datasets), more accurate, and faster pipeline for heartbeat detection in environments with high levels of noise.

Focusing on the second objective, we found that *Cd-I-W* (Dataset 1) and *WT* (Dataset 2) pipelines had the most consistent performance across different SNR levels (see Figure 3-6 and Figure 3-7). This was also noteworthy to observe that all *WT*, *Cd-W*, and *Cd-I-W* pipelines were more consistent than *Cd* and *Cd-I* pipelines across various SNR scenarios in both datasets. This observation suggests that SWT can considerably enhance the consistency or noise robustness of an ECG pipeline's heartbeat detection. This finding is consistent with that of Bladazzi et al., who showed the strength of SWT as a post-processing enhancement method for fetal ECG (fECG) [70]. They concluded that not only SWT effectively improves SNR, but it also preserves QRS morphology with less distortion. Kumar et al. also represent SWT as the best technique in morphology preservation[71]. In a recent study by Dwivedi et al. [94], it was shown that EEMD, with a comparison of its combination with SWT (EEMD-SWT) increases the SNR of ECG signal from 42.66 dB to 51.69 dB, 41.82 dB to 50.85 dB, 42.99 dB to 52.02 dB and 43.01 dB to 52.04 dB in four different recordings from MIT-BIH dataset. This SNR enhancement considerably represents the effect of applying SWT as a post-processing method in ECG denoising. The superiority of SWT in denoising ECG signal in a noisy environment also supports the finding of Kumar et al., who represents SWT as the best technique for SNR enhancement [71]. However, SWT has a particular disadvantage, which is having phase shifts with respect to the original signal [69]. This phase shift is associated with the SWT scales and gets cumulative as the scale increases. Having a closer look at the results of SWT features from the *WT* pipeline from Dataset 1 in Figure 3-6, it started with d_5 as the best feature at N_1

55

but then switched to d_6 in lower SNRs (N_2, …, N_4). This result is likely to be related to the higher phase shift of projected peaks in d_6, which makes d_5 provide more accurate information in a less noisy environment. However, in a noisy environment, sharper edges of the QRS complex that are better reflected in d_6 get a better chance of being detected even though their phase shift is larger than that of d_5.

Based on these findings, the best heartbeat detection method is not consistent at different SNR levels, and different algorithms do not represent the same robustness to noise. Therefore, there is a need to estimate SNR and its expected potential change before choosing the optimal method for heartbeat detection. Marouf et al. have introduced an approach to estimate the EMG noise level approximation in ECG signals [95]. For future work, such methods can be used to first decide on the signal quality of an ECG interval and then choose the most appropriate algorithm based on the estimated SNR.

This study has some limitations, including the manual selection of the best CEEMDAN and ICA components and using the simulated EMG instead of actual EMG artifacts. In future studies, appropriate components can be automatically selected. One possible way would be to apply cross-correlation between the detected heartbeats from different components and calculate the average cross-correlation of the detected beats. The component with the highest average cross-correlation would be a good candidate for further processing. An alternative is a multi-expert approach in which all or some candidate components are organized in a voting

scheme. To mention another limitation, we were restricted to 28 sec of Lead II. In future studies with more length of data, a continuous change in SNR level by representing an evolving noise can be investigated. In addition, future studies should use actual EMG signals generated by different levels of muscular contraction. Moreover, we considered 150 ms as an acceptable distance between the actual and detected heartbeats. This choice was made to compensate for two effects: first, the instinct of feature extraction methods that introduces phase shift with respect to the original signal, and second, the moving averaging that is applied by the Pan-Tompkins algorithm (window of 150 ms), causing phase shift. This acceptable distance needs to be reduced in future studies. To this end, Zephlet or zero-phase wavelet introduced by Percival [73] would be a candidate to eliminate the phase shift problem of SWT. Another possible improvement on the chosen algorithms can be trying different ICA methods replacing fastICA to achieve higher performance.

Chapter 4

Heartbeat detection from high-density EMG electrodes on the upper arm at different EMG intensity levels using Zephlet

The content provided in this chapter is under revision in a peer-review journal. N. Heydari Beni and N. Jiang, "Heartbeat detection from high-density EMG electrodes on the upper arm at different EMG intensity levels using Zephlet," *SSRN Electron. J.*, Oct. 2022, Available at SSRN 4221592.

4.1 Introduction

This paper presents a novel approach to heartbeat detection from the upper arm. The electrode localization on the upper arm is subjected to high EMG intensity and a weak captured electric activity of the heart. We investigated the heartbeat detection performance from these electrodes in Rest and *EF* conditions introducing various EMG intensities. The primary objective was to select the optimized location of electrodes on the upper arm, considering their similarity to ECG subjected to various EMG intensities. The secondary objective was to accurately detect heartbeats from the selected channels at each of these EMG intensities. For this matter, SWT filters were replaced by the designed filters using Zephlet, and an *MDS* was also applied to incorporate information from various Zephlet coefficients. The higher the EMG intensity was, the more challenging heartbeat detection from the contaminated signal would

become. Detecting heartbeats using this method from the selected electrodes provided us with considerably high performance in terms of *SE* and *PPV* with a comparatively accurate QRS localization.

In the next section, the experimental and computational methodologies are described in detail. Section 3 presents the results of channel selection and heartbeat detection using Zephlet compared to SWT incorporated with *MDS*. Section 4 discusses the results, limitations, and direction for future work, and the conclusion is provided in Section 5.

4.2 Methods

4.2.1 Data Acquisition

Twenty participants with no known cardiac, circulatory system, blood, or lung problems, no allergy to adhesive or rubbing alcohol, and the ability to apply force with their left hand were recruited for the experiment. All the COVID-19 safety requirements were considered, and the Office of Research Ethics of the University of Waterloo approved the protocols (ORE #41252). Prior to the start of the experiment, each participant signed a written Informed Consent. The participants were seated in a chair, relaxed, and had their left hand fixed. Three 64-channel high-density surface bioelectric electrode grids were attached around the participant's left upper arm (see Figure 4-1). The 64 channels on each of the electrode grids were arranged in an 8x8 fashion, with an inter-electrode distance of 1 cm (from middle to the
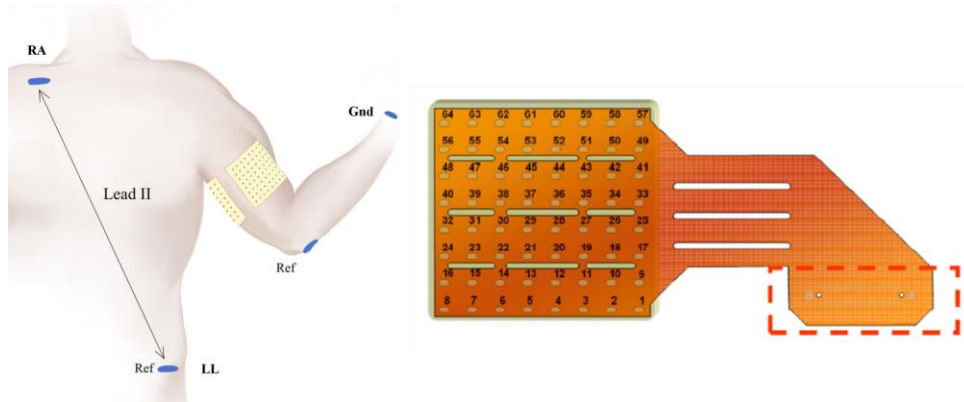
Figure 4-1. Electrode placement on the upper arm and shoulder (left) and the high-density grid (right). Three 64-electrode high density grids (in yellow) were placed on the left upper arm and their reference was placed on the left elbow. Two electrodes were placed on the right shoulder and left leg to capture Lead II. In addition, the system ground was placed on the left wrist.

middle). The reference is located on the elbow, and the ground electrode was placed on the left wrist. In addition, two disposable electrodes were placed on the right shoulder and the left hip, corresponding to the standard ECG Lead II setup.

A commercial bioelectric signal amplifier (EMG-USB2+, OT Bioelettronica, Turin, Italy) was used for signal acquisition. A hardware band-pass filter was set from 0.3 Hz to 500 Hz. The recordings were sampled at 2048 Hz and digitized with 12-bit precision. The generally acceptable frequency range of diagnostic ECG is from 0.05 to 100 Hz [23]. Therefore, the acquired data was further digitally lowpass-filtered using a third-order Butterworth filter with a cut-off frequency of 100 Hz and then downsampled to 256 Hz to reduce the computational cost.

The participants were asked to attend two different tasks: 1. Rest and 2. *EF*. Two five-minute data recording runs were recorded for the Rest task while the participants remained relaxed with no muscular contraction. In the *EF* tasks, the participants were asked to hold different weights (3.6 kg, 2.2 kg, 1.2 kg) by their left hand to produce different levels of EMG, which would be considered artifacts in the context of recording the electric information of the heart. During the recording, the contractions were isometric and isotonic, as both the joint angle and the force produced remained as constant as the participant could. Furthermore, the weights were the same across participants, making the experiment consistent and repeatable. Each weight was held for a duration of one minute and repeated three times in separate trials. The sequence of trials for all three weights (a total of nine trials) was randomized to replicate a more realistic real-time situation. Participants were provided with two minutes of rest, or more if requested, after each trial.

4.2.2 Channel Selection

We first needed to decide on how many channels should be selected for further processing. One of the main objectives of this study is electrode localization because the ultimate goal is to implement the algorithm in a wearable device on the upper arm. As such, some important factors should be considered before the selection. First of all, considering a wearable device, the fewer electrodes, the more practical the system would be. In this context, the optimal electrode number is two. Furthermore, the location of the selected electrodes

should be as consistent across the participants as possible for generalization purposes. While increasing the number of electrodes does provide us with more spatial information, we chose to set the number of electrodes to two for the above reason.

All possible pair-wise combinations from the 192 electrodes were generated, and the first 20 seconds of data from each trial (either a five-minute Rest or one-minute *EF* task) were used for training. Multivariate Regression (MVR) was then applied to these candidate pairs to predict the recorded chest ECG from lead II using the training section. The purpose was to investigate the estimation quality of each pair in estimating the ECG signal using linear regression. Pearson's Correlation Coefficient (CC) was then applied to the estimated and recorded ECG to evaluate the performance of each pair. There were 192*191 resulting CCs representing the performance of all the pairs. Finally, a 192*192 heatmap was generated to observe how the different pairs perform. The signal quality of the electrodes in the same pairs on the upper arm may change across participants, but the target was to find as consistent positions as possible across participants for generalization purposes. The heatmaps for all 20 participants were generated, and their average was calculated and projected into a single heatmap. Choosing the pair with the highest value on the averaged heatmap provided us with the most consistently informative pair across all participants. Afterwards, the grant average of the MVR coefficients corresponding to the selected pair across all trials and all participants

were considered to generate a weighted sum for further processing steps. This weighted sum produces the synthesized ECG.

4.2.3 Feature Extraction

To detect the heartbeats from the contaminated ECG signal, Zephlet was applied and then compared with SWT. The detail of each of these two algorithms is described more in detail as follows.

4.2.3.1 SWT

Applying a five-level SWT decomposes the signals into five details and one approximation coefficients, as shown in Figure 4-2. The coefficients at each scale are called a component. Based on the sampling rate, which was changed to 256 Hz, the frequency content of these six components would be 64-128 Hz, 32-64 Hz, 16-32 Hz, 8-16 Hz, and 4-8 Hz for detail coefficients one to five, respectively, and 0-4 Hz for the approximation coefficients.

4.2.3.2 Zephlet

The phase shift that SWT causes is carried along with the scales and gets cumulative as the scale increases. Therefore, the last detail and the approximation coefficients would have the most phase shifts compared to the original input signal. This phase shift may cause progressively losing more information on higher scales. Instead, the Zephlet transform maintains the phase of coefficients at all the scales with respect to the original (see Figure 4-2).
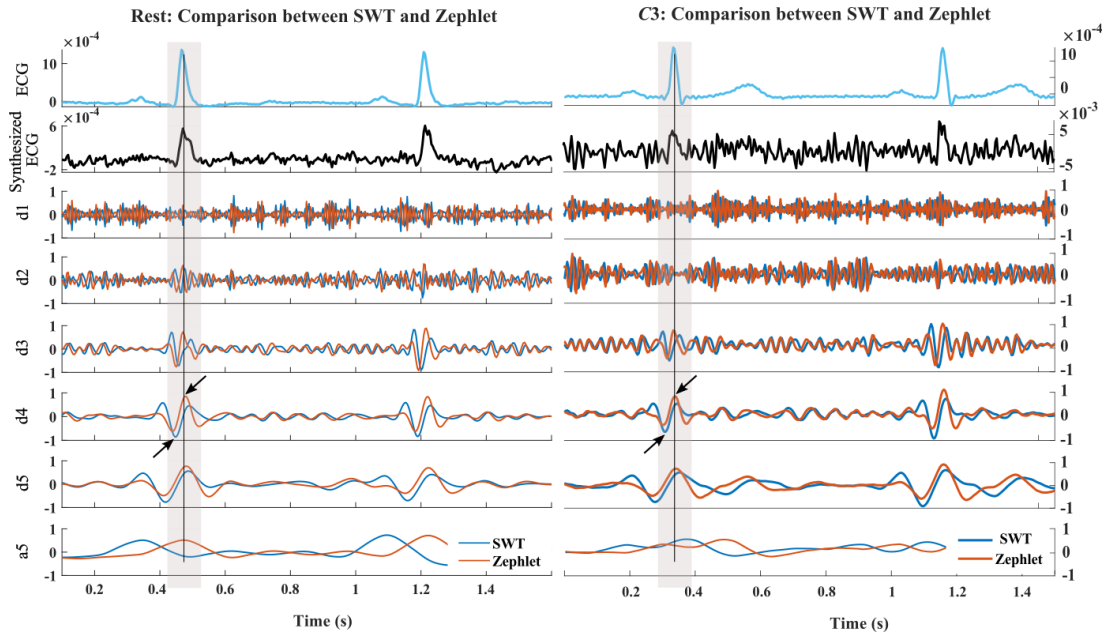
Figure 4-2. The details (d₁.d₅) and approximation (a₅) from applying SWT and Zephlet on the synthesized ECG. The elimination of phase shift in Zephlet compared to SWT can be seen in the rectangle. The black arrows represent the R- peak projections in the fourth detail (d₄) for SWT and Zephlet.

Two black arrows in the figure represent the R- peak projections in the fourth detail (d4) for SWT and Zephlet. As shown, Zephlet maintains the exact temporal location of the R-peak. On the contrary, SWT has a cumulative phase shift as the scale increases. This synchronization of Zephlet provides the opportunity to elaborate on all the components to extract meaningful information.

Zephlet is an orthogonal DWT based on zero-phase filters [73].

Expanding on the properties of Wavelet filter, h, we have:

1. Zero summation:

$$\sum_{l=0}^{L\text{-}1} h_l = 0 \tag{4-1}$$

2. Unit energy:

$$\sum_{l=0}^{L\text{-}1} h_l^2 = 1 \tag{4-2}$$

3. Orthogonality to even shifts:

$$\sum_{l=0}^{L\text{-}1} h_l h_{l+2n} = 0, \ n\text{=any nonzero integer} \tag{4-3}$$

Properties 2 and 3 provide orthonormality, which is challenging to achieve. The orthogonality to even shifts implies that the filter should be even-length. Deriving the discrete Fourier transform (DFT) of the wavelet filter h we have:

$$H(f) \equiv \sum_{l=0}^{L\text{-}1} h_l\, e^{-i2\pi fl} \tag{4-4}$$

By definition:

$$\mathcal{H}(f) \equiv |H(f)|^2 \tag{4-5}$$

Given the wavelet filter, h, is orthonormal, it can be shown that for all f:

$$\mathcal{H}(f) + \mathcal{H}(f + \frac{1}{2}) = 2 \tag{4-6}$$

The scaling filter, g, can be created using h as follows:

$$g_l \equiv (-1)^{l+1} h_{L-1-l} \tag{4-7}$$

The scaling filter shares the orthonormality property with the wavelet filter. Therefore,

$$\sum_{l=0}^{L-1} g_l^2 = 1 \tag{4-8}$$

$$\sum_{l=0}^{L-1} g_l g_{l+2n} = 0, \, n = \text{any nonzero integer} \tag{4-9}$$

And by definition:

$$\mathcal{G}(f) \equiv |G(f)|^2 \tag{4-10}$$

The squared gain function, $\mathcal{G}(.)$ satisfies:

$$\mathcal{G}(f) = \mathcal{H}(f + \frac{1}{2}) \tag{4-11}$$

Therefore, as an equivalent to the orthonormality property, we have:

$$\mathcal{G}(f) + \mathcal{H}(f) = 2 \tag{4-12}$$

Zero-phase filters should be odd-length ($L=2M+1$) and symmetrical to the center so that $a_{-l}=a_l$ for $l = -M, ..., M$. The phase of the wavelet filters cannot be zero considering their even length. Considering the importance of reducing the phase shift in these filters, Daubechies introduced the least asymmetric filters. Later, Percival introduced Zephlet as a possibility of generating zero-phase filters whose squared gain functions are consistent with Daubechies but have exactly zero phases as follows [73]:

Let $\bar{g}_l$ and $\bar{h}_l$ be inverse DFTs of the sequence $\mathcal{G}^{1/2}(\frac{k}{N})$ and $\mathcal{H}^{1/2}(\frac{k}{N})$:

$$\bar{g}_l \equiv \frac{1}{N} \sum_{k=0}^{N-1} \mathcal{G}^{1/2}(\frac{k}{N}) e^{i2\pi kl/N}, \, l = 0, 1,..., N\text{-}1 \tag{4-13}$$

$$\bar{h}_l \equiv \frac{1}{N} \sum_{k=0}^{N-1} \mathcal{H}^{1/2}(\frac{k}{N}) e^{i2\pi kl/N}, \, l = 0, 1,..., N\text{-}1 \tag{4-14}$$

Let the filters $\bar{g}_l$ and $\bar{h}_l$ be related as follows:

$$\bar{g}_l = (-1)^l \bar{h}_l \tag{4-15}$$

It can then be proven that the following requirement for orthonormality holds:

$$\mathcal{G}(\frac{k}{N}) + \mathcal{H}(\frac{k}{N}) = 2, \text{ for all } \frac{k}{N} \tag{4-16}$$

Replacing k in $\mathcal{H}\left(\frac{k}{N}\right)+\mathcal{H}\left(\frac{k}{N}+\frac{1}{2}\right)=2$ with $k+\frac{N}{2}$, we have $\mathcal{H}\left(\frac{k}{N}+1\right)+\mathcal{H}\left(\frac{k}{N}+\frac{1}{2}\right)=2$;

Therefore, $\mathcal{H}\left(\frac{k}{N}\right)=\mathcal{H}\left(\frac{k}{N}+1\right)$, meaning that $\mathcal{H}^{1/2}\left(\frac{k}{N}\right)$ is a periodic sequence with a period of N. Considering the assumption of $\mathcal{H}\left(.\right)$ being an even function, it can be shown that $\bar{h}_l$ is real-valued:

$$\bar{h}_l^{\,*}=\frac{1}{N}\sum_{k=0}^{N-1}\mathcal{H}^{1/2}(\frac{k}{N})e^{i2\pi kl/N}=\frac{1}{N}\sum_{k=0}^{N-1}\mathcal{H}^{1/2}(-\frac{k}{N})e^{i2\pi kl/N}=\frac{1}{N}\sum_{k=-(N-1)}^{0}\mathcal{H}^{1/2}(\frac{k}{N})e^{i2\pi kl/N}$$

$$=\frac{1}{N}\sum_{k=0}^{N-1}\mathcal{H}^{1/2}(\frac{k}{N})e^{i2\pi kl/N}=\bar{h}_l$$

Therefore, $\bar{h}_l$ is real-valued and $\bar{g}_l$ is also real-valued with a squared function similar to g_l and zero-phase.

The schematic diagram of Zephlet can be found in Figure 4-3. The wavelet filters are driven from the least asymmetric filters, which in this paper was chosen to be Symlet6. The Symlet6 filters and the corresponding Zephlet filters are also shown in Figure 4-3. The elimination of phase shift in Zephlet compared to SWT in all the components can be seen in Figure 4-2.
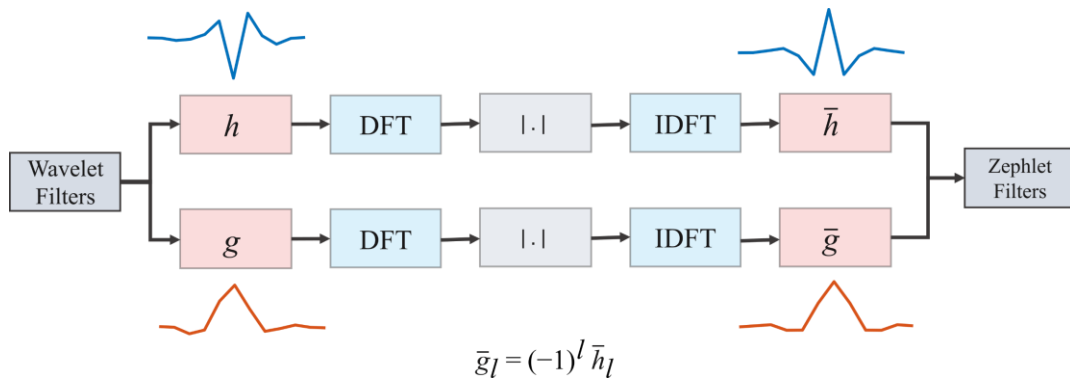
Figure 4-3. The schematic diagram of deriving Zephlet filters based on Wavelet filters. The symlet6 highpass (in blue) and lowpass (in red) filters before and after applying Zephlet are represented.

4.2.4 *MDS* to Merge Component Information

The dominant frequency content of the QRS complex lies under 21 Hz, and a wide range of studies have focused on only that frequency range for QRS detection. However, a much wider frequency range of 0.1-100 Hz has an important diagnostic value. Therefore, our analysis considered all the corresponding components to this wider frequency range. Only the last component from each method, which contains baseline wanders and movement artifacts, was discarded, and we included five components in SWT and Zephlet in the subsequent analyses.

In order to merge information from the five components, we designed an *MDS* to increase heartbeat detection accuracy. First, the classic Pan-Tompkins algorithm with some adaptations [96] was applied to each of the components individually. A series of QRS complexes were detected from each component, respectively. Then we used a 200-ms non-

69

overlapping moving window for merging the detected beats from all five series. The window

length was chosen to be 200 ms because it is physiologically impossible for two consecutive

QRS complexes to occur within 200 ms [97]. The *MDS* scheme was applied, in which a

minimum of three positively voting components (chosen empirically) would lead to a final

positive detection for the current window. The location of the detected beat was set to be the

average temporal location of all positive votes. This *MDS* scheme is illustrated in Figure 4-4.
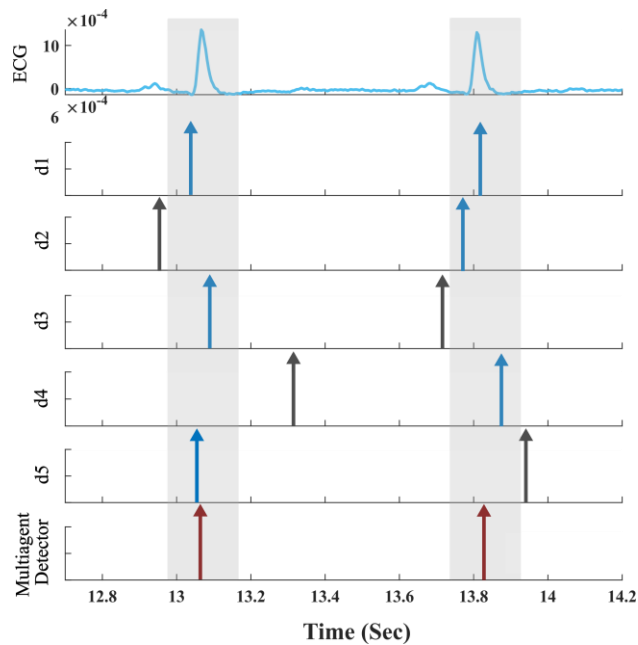
Figure 4-4. *MDS***. The output of Pan-Tompkins applied to different details (d_1-d_5) is illustrated. An example of the moving window is shown in grey rectangle. The blue arrows lie within the window and the grey ones are outside, so they are withdrawn by the *MDS*. In the first window, if we wanted to only consider either d_2 or d_4, we would have lost that heartbeat. The same logic holds for the second window with d_3, and d_5. But this system prevents such losing of information. Furthermore, the location of the *MDS* output, which is shown in the last row by red arrows is the average of all the blue arrow from the detail outputs.**

After the entire trial was processed, a further refractory rejection period scheme was also applied to the final detected heartbeats with a temporal distance of less than 200 ms: the mid-point of the temporal positions of two consecutive beats within 200 ms was used as the temporal location of the merged beat.

4.2.5 Performance Evaluation and Statistical Analysis

SE, *PPV*, and F_1 score were calculated to evaluate the performance of the methods in heartbeat detection:

$$SE = \frac{TP}{TP+FN} \tag{4-17}$$

$$PPV = \frac{TP}{TP+FP} \tag{4-18}$$

$$F_1 = \frac{2 \times PPV \times SE}{PPV+SE} \tag{4-19}$$

where *TP* or true-positive is the number of beats that were detected within a pre-defined distance from an actual heartbeat (from the Lead II ECG). This tolerance was initially set to 50 ms but then progressively reduced to 20 ms with a step of 10 ms to investigate the temporal accuracy of the detection. *FP* or false positive is the number of false detections, and *FN*, *i.e.* false negative, represents the number of missed heartbeats. *SE* determines how well an algorithm can detect heartbeats, and *PPV* demonstrates the precision of the detection. The F_1 score is used to compare the algorithms considering both the *SE* and *PPV as* a measure of accuracy.

4.3 Results

4.3.1 Channel Selection

The performance of different pairs in estimating ECG (in terms of *CC*) using MVR is represented as a 192*192 heatmap averaged over 20 participants and two Rest sessions, as shown on the left side of the first row of Figure 4-5. The pair of channels providing the highest and the second-highest *CC* values were (8, 128) with $CC = 0.72$ and (8, 120) with $CC = 0.71$. The neighbouring channels of 8 and 120 provided comparatively higher and more robust *CC* compared to the other pair. Therefore, choosing the pair (8, 120) for the Rest sessions would provide higher performance robustness in case of positional shift due to error or implementation limitations. The location of this pair on the upper arm is illustrated on the right side of the first row in Figure 4-5. Following the same analysis, the best pair for all the *EF* conditions were selected as pair (56, 120), as shown on the right side of the first row in Figure 4-5.

The averaged weights achieved from applying MVR on the selected two channels over training trials and sessions were calculated for each participant. Utilizing the resulting coefficients, we formed a synthesized ECG for each participant for further processing steps in test trials in each condition. A sample of the synthesized ECG, along with the two selected channels and Lead II in Rest and *EF* conditions, are shown in Figure 4-6.

72
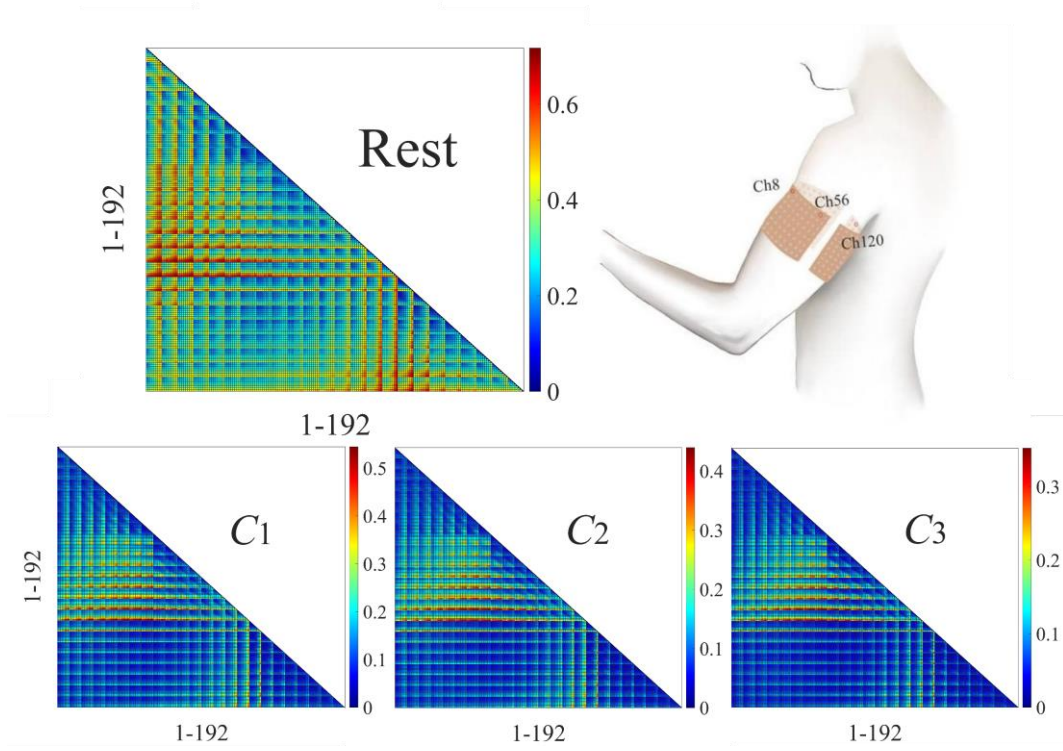
Figure 4-5. The *CC* between the estimated ECG and chest ECG using different pairs in Rest and MC conditions with the respective selected locations on the upper arm. Top left: Rest; Top right: the respective positions of the electrodes 8, 56 and 120, on the upper arm. Bottom left: contraction level 1 (*C*1), Bottom middle: contraction level 2 (*C*2), Bottom right: contraction level 3 (*C*3).
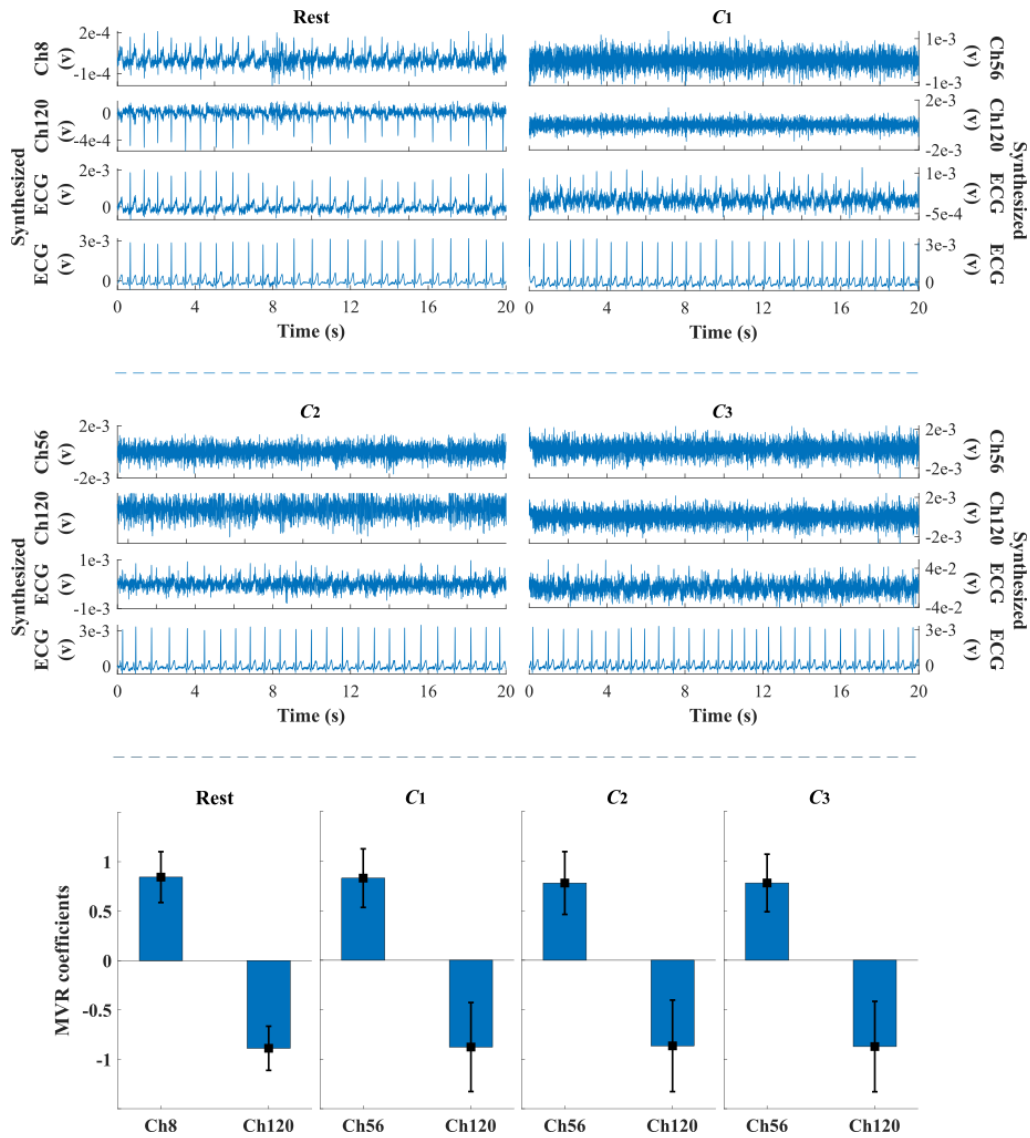
Figure 4-6. Top: An example of the selected channels in Rest (channels 8 and 120) and *EF* (channels 56 and 120) conditions along with the resulting synthesized ECG and Lead II at each condition. As illustrated, the peaks are mostly not visually identifiable in the channels 8, 56, and 120, however, they become clearly identifiable in the synthesized ECG. Bottom: The average normalized MVR coefficients for channels 120 and 8 in Rest and channels 56 and 120 for *EF* conditions. As illustrated, these two channels behave opposite across the subjects and sessions.

74

4.3.2 Heartbeat detection

The *SE* and *PPV* for Zephlet and SWT after applying *MDS* with various tolerance level (T_1-T_4) considerations averaged on 20 participants, two sessions, and 14 trials from the Rest sessions are represented in the first row of Figure 4-7. The first trial of 15 trials was eliminated as it was used for channel selection purposes. Both algorithms suffered a reduction in performance for lower tolerances. *SE* reduced from 0.94 ± 0.16 to 0.81 ± 0.2 for Zephlet and from 0.87 ± 0.19 to 0.31 ± 0.25 for SWT at T_1-T_4. Meanwhile, *PPV* followed the same pattern as *SE* for both algorithms. It reduced from 0.94 ± 0.16 to 0.81 ± 0.2 for Zephlet, and from 0.88 ± 0.18 to 0.31 ± 0.25 for SWT. However, it's evident from the figure that Zephlet attained consistently and significantly better performance ($p<0.01$) compared to SWT at all the tolerance levels in both *SE* and *PPV* terms. Incorporating both *SE* and *PPV*, the F_1 score of Zephlet was 0.81 ± 0.2, 0.9 ± 0.19, 0.93 ± 0.17 and 0.94 ± 0.16 respectively for T_1-T_4. On the other hand, SWT provided an F_1 score of 0.31 ± 0.25, 0.46 ± 0.25, 0.75 ± 0.19, and 0.87 ± 0.18, respectively, for T_1-T_4, representing a significantly lower performance at all the levels.

The performance of both algorithms is affected under noisy conditions, which is the *EF* sessions from level 1 to 3 (C_1-C_3) in this study. The comparison of Zephlet and SWT after applying *MDS* was made using the F_1 score for each contraction level, and the averaged results over 20 participants, two sessions, and two trials were investigated and represented in the

second row of Figure 4-7. The first trial of 3 trials was eliminated as it was used for channel selection purposes. The results were also compared to the Rest condition (see the second row of Figure 4-7).
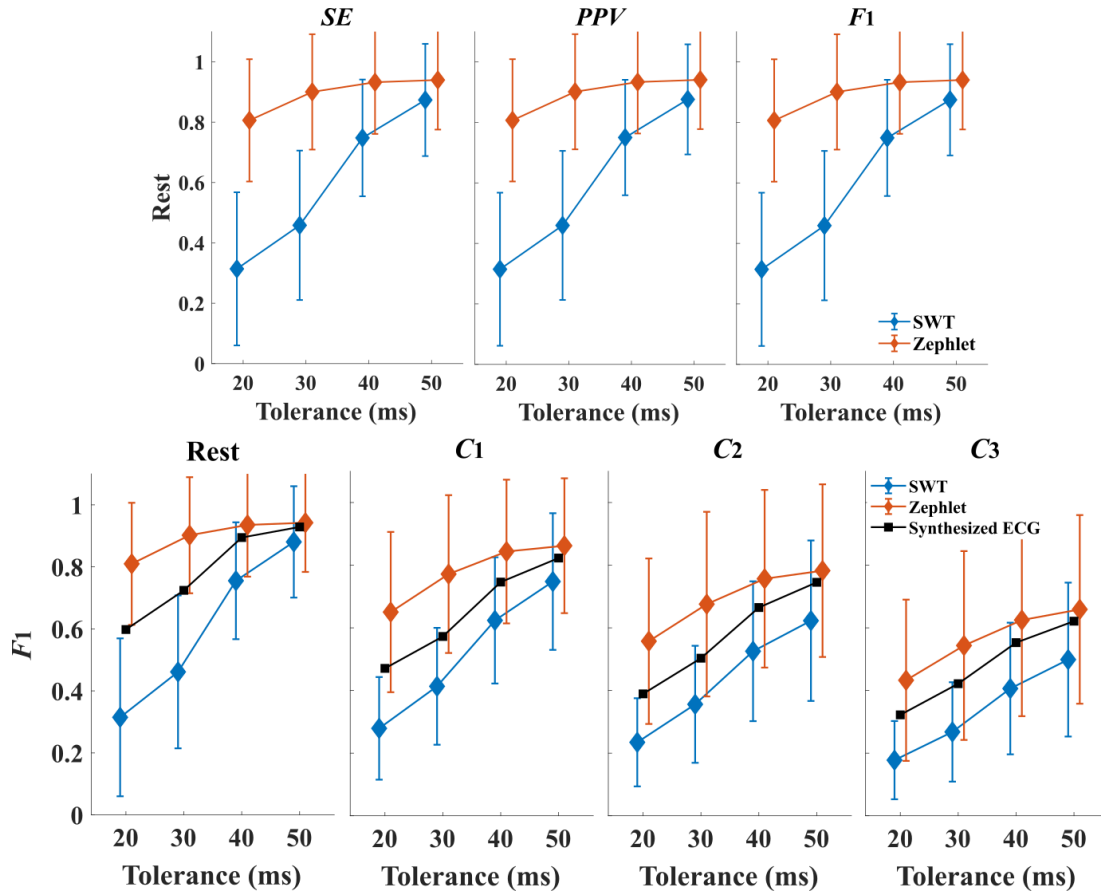
Figure 4-7. First row: The performance of Zephlet (orange) and SWT (blue) in terms of *SE*, *PPV*, and F_1 score from T_1 to T_4 in the Rest. Second row: The performance of Zephlet (orange) and SWT (blue) compared to synthesized ECG (black) in terms of F_1 score for Rest and *EF* conditions. The performance of both the algorithms decrease as the level of contraction increases at all conditions. However, Zephlet was consistently and significantly better than SWT in terms of F_1 score (T_1-T_4) and better than (T_1-T_3) or equal to (T_4) synthesized ECG.

At T_1, the F_1 score of Zephlet was 0.66 ± 0.26, 0.57 ± 0.26, and 0.44 ± 0.26 for C_1 to C_3, respectively. According to t-test, SWT provided a significantly lower F_1 score by 0.28 ± 0.16, 0.24 ± 0.14, and 0.19 ± 0.13 for C_1 to C_3, respectively. At T_2, the F_1 score of Zephlet was 0.77 ± 0.26, 0.69 ± 0.29, and 0.56 ± 0.31 and significantly better ($p<0.01$) than SWT with 0.41 ± 0.19, 0.36 ± 0.19, and 0.28 ± 0.16 for C_1 to C_3, respectively. At T_3, the F_1 score of Zephlet was 0.85 ± 0.23, 0.77 ± 0.28, and 0.64 ± 0.31 for C_1 to C_3. On the other hand, SWT had a significantly lower ($p<0.01$) F_1 score of 0.62 ± 0.2, 0.53 ± 0.22, and 0.42 ± 0.21, respectively for C_1 to C_3. Finally, at T_4, the F_1 score of Zephlet was 0.86 ± 0.22, 0.79 ± 0.26, and 0.67 ± 0.31 and significantly better ($p<0.01$) than SWT with 0.75 ± 0.22, 0.64 ± 0.25, and 0.50 ± 0.25 for C_1 to C_3, respectively. As expected, the performance of both algorithms reduced as the level of muscle contraction increased, and it is significantly lower than the Rest condition at all T_1-T_4, as shown in Figure 4-7. The superiority of Zephlet over SWT in all EF conditions confirms the results achieved in the Rest condition.

The F_1 score for both algorithms was then compared to Pan-Tompkins applied to the synthesized ECG without any further feature extraction. As illustrated in Figure 4-7, Pan-Tompkins provides a significantly better F_1 score than SWT ($p<0.01$) at all tolerance levels. However, Zephlet gains a significantly higher F_1 score at T_1-T_3 ($p<0.01$) compared to Pan-Tompkins. At T_4, both Zephlet and Pan-Tompkins provide statistically same F_1 score ($p = 0.16$, $p = 0.18$, $p = 0.3$, and $p = 0.33$, respectively for T_1-T_4). These results indicate the importance

of using Zephlet incorporated with *MDS* as an effective feature extraction method for more accurate detection and localization of heartbeats.

4.3.3 Generalization of MVR Coefficients

The averaged coefficients from applying MVR on the selected two channels over subjects, trials, and sessions were calculated for Rest and *EF* conditions. At the Rest condition, the average coefficients for channels 8 and 120 were 3.078 and -2.8, respectively. At C_1, the average coefficient was 2.02 for channel 56 and -2.12 for channel 120. The coefficients changed to 1.46 for channel 56 and -1.55 for channel 120 at C_2. Finally, at C_3, the coefficients were 75.44 for channel 56 and -80.48 for channel 120. The normalized coefficients are presented in Figure 6. As illustrated, these two coefficients consistently have an opposite sign with highly similar values across all the conditions, meaning the two hotspots are showing an opposite behaviour in estimating Lead II, which indicates a difference in the phase of ECG-related information (close to 180 degrees) at the two hotspots. Considering this, we regenerated the synthesized ECG using updated weights equal to 1 for channels 8 and 56 and -1 for channel 120. This update helps with further generalization over muscle contraction intensity levels.

All the results were repeated using these generalized coefficients, and there was no significant change ($p>0.1$ for all the tolerance levels and conditions) in either SWT or Zephlet results. The F_1 score at Rest was 0.81 ± 0.20, 0.9 ± 0.19, 0.94 ± 0.17, and 0.94 ± 0.16 for Zephlet, and 0.31 ± 0.25, 0.46 ± 0.25, 0.76 ± 0.19 and 0.88 ± 0.18, for SWT, respectively for

$T_1 - T_4$. Even though these results were not significantly different ($p>0.1$) compared to those of the original weights, the STDs were lower in the generalized version. At C_1, the F_1 score was 0.65 ± 0.26, 0.77 ± 0.25, 0.84 ± 0.23, and 0.86 ± 0.22 for Zephlet, and 0.28 ± 0.16, 0.41 ± 0.19, 0.62 ± 0.2, and 0.75 ± 0.22 for SWT, for $T_1 - T_4$, respectively. At C_2, the F_1 score was 0.56 ± 0.26, 0.68 ± 0.29, 0.76 ± 0.28, and 0.78 ± 0.28 for Zephlet, and 0.23 ± 0.14, 0.36 ± 0.19, 0.53 ± 0.22 and 0.62 ± 0.26, for SWT, respectively for $T_1 - T_4$. At C_3, the F_1 score was 0.43 ± 0.26, 0.54 ± 0.3, 0.62 ± 0.31, and 0.66 ± 0.3 for Zephlet, and 0.18 ± 0.12, 0.27 ± 0.16, 0.41 ± 0.21, and 0.5 ± 0.25 for SWT, respectively for $T_1 - T_4$.

Therefore, not only the best position of electrodes but also the weight of these electrodes in generating the synthesized ECG can be generalized across the participant pool in Rest and *EF* conditions. Furthermore, the generalized weights are consistent at Rest and *EF* conditions.

4.4 Discussion

Accurate identification of cardiac arrhythmias can prevent a significant number of global deaths related to these conditions. Such an identification can be performed using wearable devices that acquire cardiac electrical activity from the body surface to provide constant cardiac monitoring [1]. Studies that are focused on extracting cardiac information from electrical activity recorded from the body surface can be categorized into two main groups: the choice of alternative electrode placement and the development of ECG processing algorithms.

The present study was designed for heartbeat detection using the signals recorded from the upper arm. The first objective of the study was to identify the optimal electrode locations on the upper arm by means of high-density surface recording (a total of 192 electrodes) to provide the best information for cardiac activity. The second objective of this study sought to detect heartbeats from the selected channels using a zero-phase wavelet (Zephlet) incorporated with an *MDS*. The investigation was done under two main conditions: Rest and *EF,* to evaluate the performance of the system using contaminated signals by different EMG intensity levels.

With respect to the first research question, we identified one pair of electrodes for Rest (120,8) and another pair for *EF* (120,56) conditions to be providing the most information regarding cardiac activity (see Figure 4-5). As illustrated, the location of one electrode (120) does not change from Rest to different muscle contraction levels. However, the location of the other selected electrode shifts mostly around the longitudinal axis after muscle contraction (from Rest to C_1). This change suggests that frontal electrodes are more affected than lateral electrodes during muscle contraction (see Figure 4-5). However, the level of contraction (C_1-C_3) does not change the location of the selected pair. Instead, the contraction only causes the information to concentrate more on the selected pair rather than their neighbouring area, as illustrated in Figure 4-5. These findings suggest that future studies consider a total of three electrodes while designing a wearable device on the upper arm.

Very little was found in the literature on the question of which locations on the upper arm provide more information related to ECG. Escalona *et al*. performed a study in which they investigated and compared the SNR of various bipolars composed of 10 electrodes recorded from the wrist, forearm, and upper arm. They identified the highest SNR related to a bipolar composed of the upper arm and wrist electrodes. The next best electrode pair was related to the combination of the upper arm and forearm electrodes, and after that, the best bipolar was composed of two electrodes from the upper arm. The first two options require a two-piece wearable or one large enough wearable to cover a significantly big portion of the arm, which suffers from low wearability. Therefore, the combination of upper arm channels proposed in the current study is comparatively more appealing. Furthermore, the rough location of these two electrodes on the upper arm is consistent across all conditions investigated in this study (Figure 4-5). The present results are promising in at least three major aspects. Firstly, the spatial location of selected electrodes is significantly more precise considering the large number of recording electrodes (192) placed on the upper arm at a distance of 1 cm from each other. Secondly, the selected best positions were also consistent across all 20 subjects. And lastly, the best pair was chosen for both Rest and *EF* conditions separately, including four total muscle contraction levels (Rest, C_1-C_3). Although chest ECG signals were used for identifying these electrode locations, they were no longer required in future studies because of the above consistencies. And the above properties provide inherent robustness across intra-subject, inter-

subject and inter-contraction variabilities, all of which are highly valuable for practical applications.

Focusing on the second research question, we generated a synthesized ECG using the selected pair for further analysis. The synthesized ECG was first estimated using a weighted sum of the pair of electrodes. The two electrodes within this pair consistently had opposite behaviour across subjects. Therefore, the synthesized ECG was later set to the subtraction of the two monopolar channels (see Figure 4-6). This opposite behaviour was consistent with the previously mentioned study by Escalona *et al.*[10].

The accurate localization of QRS complexes plays an important role in estimating heart rate and heart rate variability. However, the reported accuracy of heartbeat detection in the literature is broadly lacking information regarding tolerance or the maximum accepted distance between the detected and actual heartbeats. Therefore, there is very limited attention given to reducing this tolerance further to increase the performance of the heartbeat detection algorithms. For instance, the phase shift between the detail coefficients and the original signal that is caused by the commonly used SWT (especially in higher scales) has been widely ignored. We applied Zephlet at the level of five to decompose the synthesized ECG to a series of detail and approximation coefficients that have complete synchrony with respect to the original signal. Furthermore, it should be considered that this phase shift causes the detail coefficients not to be synchronized with each other as well. Therefore, the detected heartbeats

from different detail coefficients are not aligned with each other, even though they represent a single heartbeat. This prevents the opportunity of incorporating the detected heartbeats from different detail coefficients. On the other hand, most of the studies have only focused on the frequency range under 50 Hz for the means of QRS detection. They have selected only several of the wavelet details for heartbeat detection by reconstructing the signal using the selected components [2], or they have only used one component for heartbeat detection [63]. However, the QRS complexes contain information up to 100 Hz, and if the detail coefficients are synchronized, combining information from all of them can be an advantage in the detection. In support of this, our previous study shows that all scales of the detail coefficients (2 Hz - 128 Hz) are highly informative regarding heartbeat detection [72]. Hence, the importance of including all the detail coefficients and extracting meaningful information from them indicates another valuable aspect of eliminating this phase shift and using Zephlet instead of SWT. As described in the results section, the synchronization of details allowed us to incorporate Zephlet with an *MDS* and significantly increased the performance of heartbeat detection at all tolerance levels. Furthermore, the superiority of Zephlet compared to SWT, which gets more pronounced as the tolerance decreases, highlights the negative effect of SWT phase shift and importance of reporting the tolerance along with the accuracy in future studies (see Figure 4-7).

This study has some limitations, including the necessity to choose a pre-defined mother wavelet. There is abundant room for optimizing this mother wavelet to better fit our criteria

which is improving the performance of heartbeat detection. Moreover, different detail coefficients get the same weight in voting for the presence or absence of a heartbeat in the current *MDS*. A more sophisticated weight scheme can be further developed, considering the possibility of a clearer QRS complex projection at some of these detail coefficient levels. And lastly, the heartbeat detection methodology that is used in this study is the very popular Pan-Tompkins algorithm in the literature [83], [96]. Despite the promising results of this algorithm, alternative detection algorithms should be investigated in future studies.

Chapter 5

ECG delineation from the upper arm using mother wavelet optimization incorporated with Zephlet at four EMG contamination levels

The content provided in this chapter is ready to submit to a peer-review journal. N. Heydari Beni, N. Jiang, "ECG delineation from the upper arm using mother wavelet optimization incorporated with Zephlet at four EMG contamination levels."

5.1 Introduction

The current study presents a novel approach to obtaining the optimal mother wavelet in ECG delineation in high interference and low SNR scenarios, such as signals from the upper arm. The exact electrode localizations on the upper arm were defined based on our previous study through the analysis of high-density surface recordings [98]. We applied Zephlet to synthesized ECG compound of these selected electrodes to extract features with the highest similarity of averaged PQRST to Lead II. In this study, we parametrized the Zephlet mother wavelet to increase the ECG delineation performance of the selected component in the Rest condition and *EF* condition with high EMG artifacts. Mother wavelet parametrization gave us the opportunity to generate multiple wavelet filters by changing the varying parameters. Following that, we selected the mother wavelet with the highest performance in PQRST

delineation per subject and condition. Finally, we investigated the possibility of generalizing the mother wavelet for ECG delineation over subjects and various EMG intensity levels.

In the next section, the experimental and computational methodologies are described in detail. Section 3 presents the results of feature selection, mother wavelet optimization, and PQRST delineation using the optimized mother wavelet. Section 4 discusses the results, limitations, and direction for future work, and the conclusion is provided in Section 5.

5.2 Methodology

5.2.1 Data Acquisition

Twenty participants, self-reported as healthy, were recruited for the experiment. All the COVID-19 safety protocols were considered and approved by the Office of Research Ethics of the University of Waterloo (ORE #41252). All participants signed a written Informed Consent prior to starting the experiment. The participants were seated in a chair, relaxed, and had their left hand fixed. The left upper arm of the participants was covered with three 64-channel surface bioelectric electrode grids (shown in Figure 5-1). The 64 channels on each of the electrode grids were arranged in an 8x8 fashion, with an inter-electrode distance of 1 cm. The reference was located at the elbow. Additionally, two disposable electrodes were placed on the right shoulder and left hip in accordance with the standard setup for an ECG Lead II.
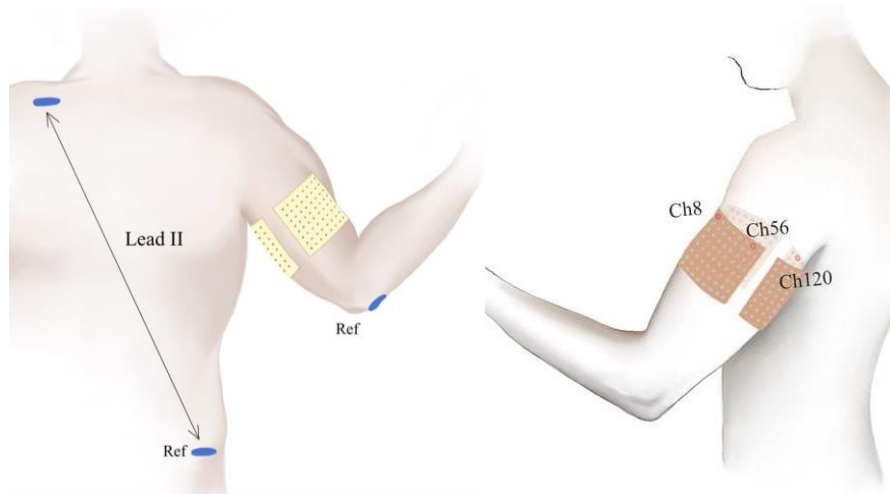
Figure 5-1 . Electrode placement on the upper arm and shoulder (left) and the selected positions (right). Left: three 64-electrode high density grids (in yellow) were placed on the left upper arm. One electrode was placed on the right shoulder having the reference on the left hip to capture Lead II. Right: the selected positions including electrodes 8, 56 and 120, on the left upper arm. Electrodes 8 and 120 were selected for Rest and electrodes 56 and 120 were selected for muscle contraction conditions.

The signal acquisition was performed using OT Bioelettronica's EMG-USB2+ bioelectric signal amplifier. Hardware band-pass filtering was done from 0.3 Hz to 500 Hz, and data were sampled at 2048 Hz and digitized with 12-bit precision. The acquired data was further digitally lowpass-filtered using a third-order Butterworth filter with a cut-off frequency of 100 Hz (considering the acceptable frequency range of diagnostic ECG from 0.5 to 100 Hz [23]). Finally, data were downsampled to 256 Hz to reduce the computational cost.

The experiment included two conditions: Rest and *EF*. Rest condition included two five-minute data recording runs while the participants remained relaxed with no muscular contraction. In the *EF* condition, the participant was asked to hold different weights (C_1:1.2

kg, C_2: 2.2 kg, C_3: 3.6 kg) with the left hand, producing different intensity levels of EMG. The intention of generating various intensities of EMG was to contaminate the recording cardiac electrical information with these artifacts, replicating real-life scenarios. Participants performed isometric and isotonic contractions during recording, maintaining a 90-degree elbow angle while the upper limb was in a natural upright position. The same weights were used for all participants, ensuring that the experiment could be repeated and replicated. There were three separate trials of each weight for a duration of one minute each. The sequence of trials (overall nine trials for all weights) was randomized to replicate a realistic real-life situation. After each trial, two minutes of rest (or more if requested) were provided to the participants.

5.2.2 Feature Extraction

From our previous study, we selected the optimal electrode positions out of 192 for each of the Rest (channels 8, 120) and *EF* (channels 56, 120) conditions [98]. The location of these channels on the left upper arm is illustrated in Figure 5-1. Furthermore, we were able to generalize the weights of these two channels over participants, sessions, and trials [98]. Accordingly, the following equations hold for all the conditions and participants:

$$\text{Synthesized ECG at Rest} = \text{Channel 8 - Channel 120} \tag{5-1}$$

$$\text{Synthesized ECG at } \textit{EF} = \text{Channel 56 - Channel 120} \tag{5-2}$$

Next, Zephlet was applied to the synthesized ECG at Rest and *EF* to address the SWT phase shift drawback. The schematic diagram of Zephlet, along with the DWT and SWT, can be found in the third row of Figure 5-2. In Zephlet, the phase information of the wavelet filters is eliminated, resulting in achieving Zephlet filters with zero phases. Applying a 5-level Zephlet resulted in decomposing signals into five details and one approximation coefficients. Based on the sampling rate, which was reduced to 256 Hz, the frequency content of these six components was 64-128 Hz, 32-64 Hz, 16-32 Hz, 8-16 Hz, and 4-8 Hz for detail coefficients one to five, respectively, and 0-4 Hz for the approximation coefficients.

The extracted components using Zephlet have different frequency ranges, some of which have better coverage of the PQRST frequency content. To delineate the PQRST waveform, selecting the best representative detail was critical. Therefore, a training phase was required for which we used 3-fold cross-validation on each trial of the dataset. To identify the best representative feature, we first applied the Pan-Tompkins algorithm on Lead II to detect the location of the heartbeats. Due to the synchrony of Zephlet features with Lead II, the identified

89
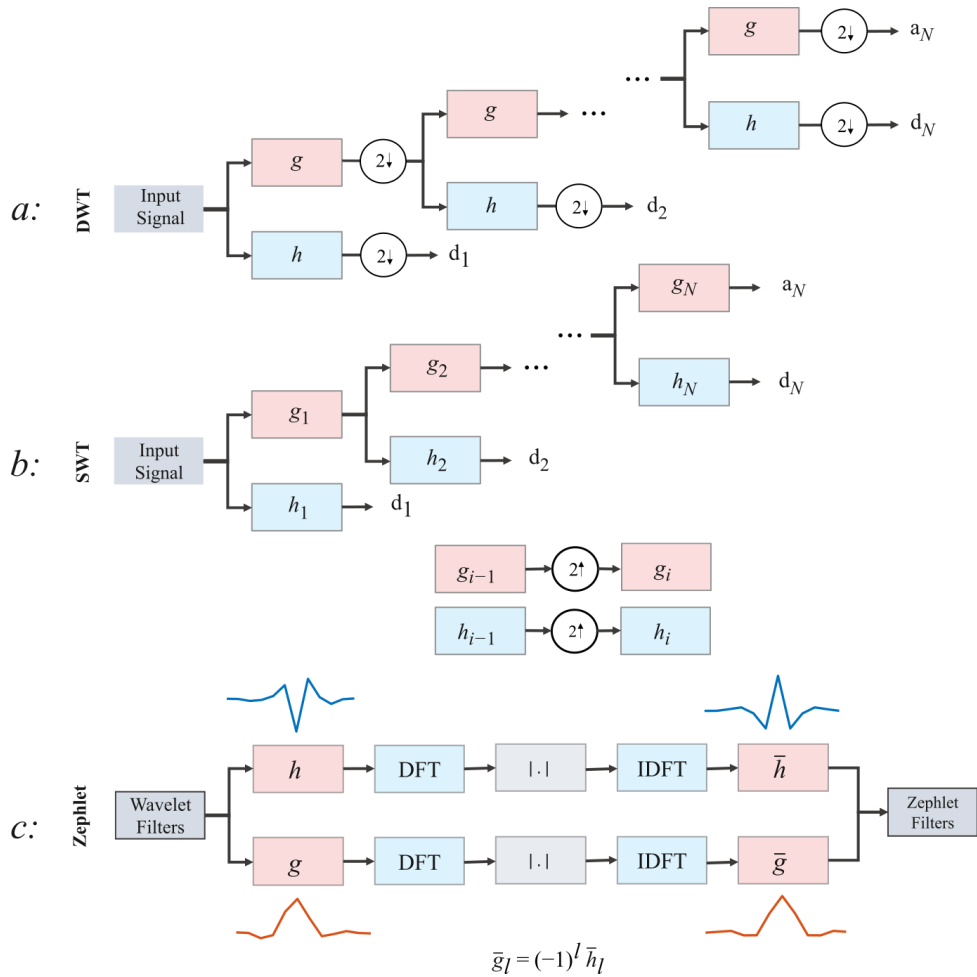
Figure 5-2. (a,b) Extracting DWT and SWT coefficients; (c) the schematic diagram of deriving Zephlet filters based on Wavelet filters. The symlet6 highpass (in blue) and lowpass (in red) filters before and after applying Zephlet are represented.

locations were common between Lead II and all Zephlet features. These R-peaks were considered given in this study because of the purpose, which was waveform delineation rather than heartbeat detection. We then segmented 0.3 seconds before and 0.4 after R-peaks as the

PQRST waveform (overall 0.7 sec). This segmentation was based on the standard length of waveforms known as P-wave: 0.2 sec, QRS complex: 0.1 sec, and T-wave: 0.3 sec. The intention was to calculate the averaged PQRST over all of the extracted heartbeat segments for lead II and then compare it with each Zephlet feature using *CC*. Two considerations were required before calculating the *CC* of the averaged PQRST of the Lead II and the components. First, the detected R-peaks using the Pan-Tompkins algorithm do not precisely align with the actual R-peak. The reasoning behind such a temporal shift is the pre-processing in the Pan-Tompkins algorithm, which includes an integration step. To address this, we first corrected the detected R-peak location by searching for the maximum amplitude within 15ms before and after the detected location. The second consideration was the phase difference between the synthesized ECG and Lead II for some individual subjects. An example of this phase shift can be seen in the averaged PQRST of Lead II and detail 4 of subject 5, as shown in Figure 5-3. The rationale behind this phase difference lies in the selected pair location on the upper arm that was generalized over all the participants [98].

This phase shift is an independent factor in the mother wavelet optimization procedure. Therefore, instead of a simple *CC*, we used a cross-correlation function between -20 ms to 20 ms with a step of 10 ms. The maximum *CC* among these five different phase shifts was considered as the performance of that specific component (second panel of Figure 5-3).

91
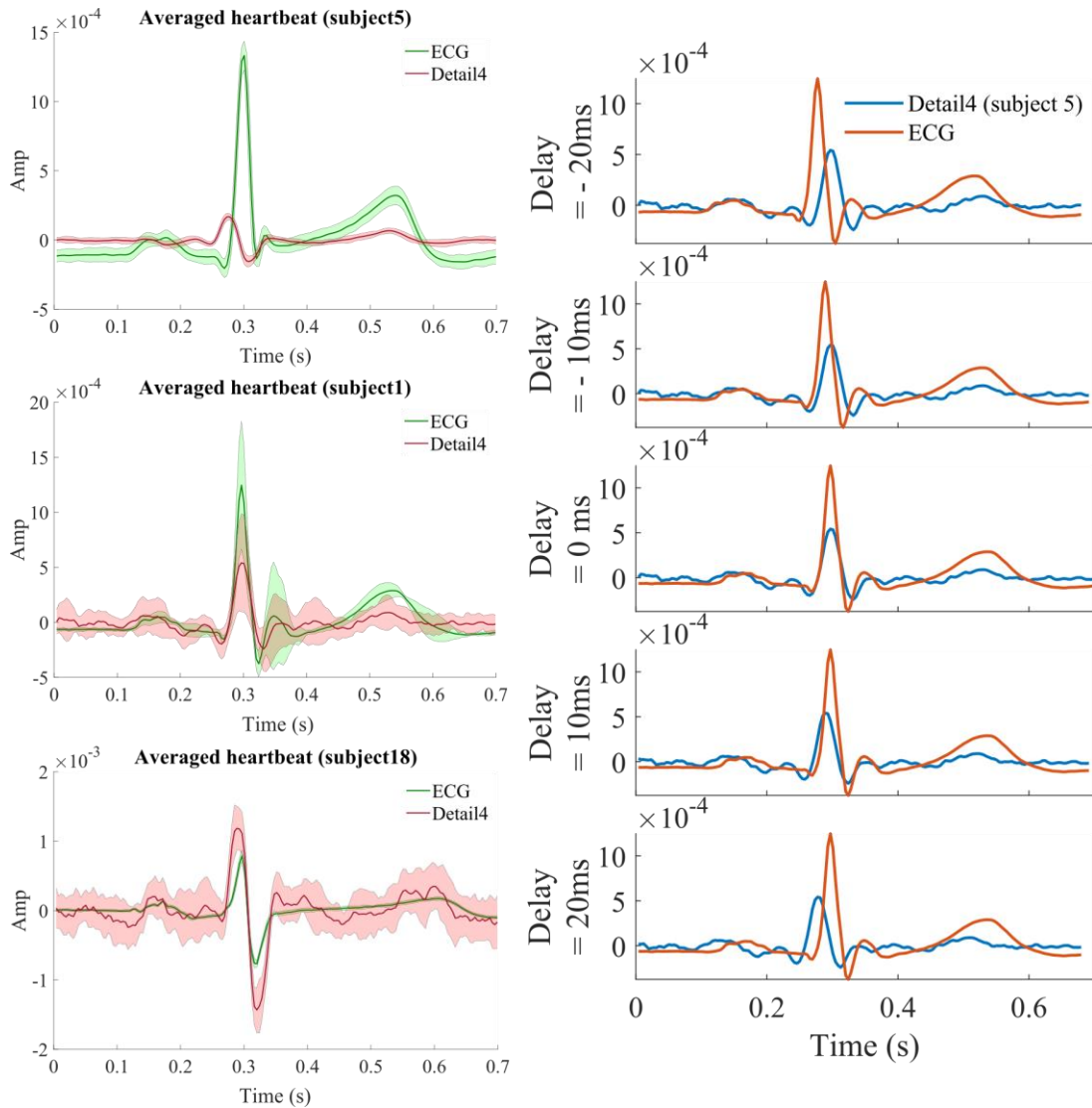
Figure 5-3. (left) Examples of the averaged heartbeats for subjects 1, 5, and 18. (right) averaged PQRST for ECG and detail4 from subject 5 having -20, 10, 0, 10, and 10 ms of delay with respect to each other.

After the selection of the best feature, the next step was to parametrize the mother

wavelet and choose the parameters providing the best performance in PQRST delineation.

5.2.3 Parametrization of the mother wavelet

In CWT, the coefficients from each frequency band are driven using the shifts of a generating function on a particular scale, ψ, *i.e.,* the mother wavelet following Eq. (5-3)

$$\psi_{a,b}(t) = \frac{1}{\sqrt{a}} \psi \left(\frac{t\text{-}b}{a}\right) \tag{5-3}$$

$$WT_{\psi}\{x\}\{a,b\} = \int_R x(t)\, \psi_{a,b}(t)\, dt \tag{5-4}$$

So, the wavelet coefficients at scale a and shift b are calculated as in Eq.(5-4). The series of coefficients at each scale is called a component. The wavelet coefficient is derived from the convolution of the signal with a filter, h, which is a derivative of the mother wavelet as follows:

$$\gamma_{jk} = \int_{-\infty}^{\infty} x(t)\, \frac{1}{\sqrt{2^j}} \psi \left(\frac{t\text{-}k\,2^j}{2^j}\right) dt \tag{5-5}$$

$$h(t) = \frac{1}{\sqrt{2^j}} \psi \left(\frac{\text{-}t}{2^j}\right) \tag{5-6}$$

Sampling $h(t)$ at points $1, 2^j, 2^{2j}, \ldots, 2^N$ yields $h[n]$, which is the highpass decomposition filter for the DWT. Based on the perfect reconstruction characteristic of wavelets, the lowpass filter will accordingly be:

$$g[k] = (\text{-}1)^{1\text{-}k} h[1\text{-}k] \tag{5-7}$$

According to Eq. (5-5) and Eq. (5-6), the highpass filter h defines the mother wavelet ψ, and also can be deduced from lowpass filter g considering the orthogonality. The

Multiresolution Analysis MRA framework defines the lowpass filter in a parameterized framework, providing an opportunity for tuning the mother wavelet based on an optimization criterion [99]. Therefore, by parametrization of the mother wavelet, the problem of choosing the mother wavelet becomes the problem of selecting a finite set of filter coefficients. The lattice parameterization described by Vaidyanathan [100] offers the opportunity to design g via unconstrained optimization [99].

With the filter g having the length of L, the number of constrictive conditions to satisfy orthogonality equals $L/2+1$. Therefore, there will be $L/2-1$ degrees of freedom remaining for designing the filter. The filter g is defined below using two parameters $[\alpha, \beta]$ for the length of $L=6$:

$$i=0,1: g[i] = \frac{[(1+(-1)^i cos\alpha + sin\alpha) \times (1-(-1)^i cos\beta - sin\beta) + (-1)^i 2sin\beta cos\alpha]}{4\sqrt{2}} \qquad (5\text{-}8)$$

$$i=2,3: g[i] = \frac{[1 + cos(\alpha - \beta) + (-1)^i sin (\alpha - \beta)]}{(2\sqrt{2})} \qquad (5\text{-}9)$$

$$i = 4,5: g[i] = \frac{1}{\sqrt{2}} - g(i - 4) - g(i - 2) \qquad (5\text{-}10)$$

Various values of $[\alpha, \beta]$ parameters in the range of $-\pi + \pi/10$ to $\pi - \pi/10$ by the step of $\pi/10$ were used to generate a total of 361 (19*19) mother wavelets resulting in 361 filter pairs to find the pair providing the highest performance in the PQRST delineation. The optimization
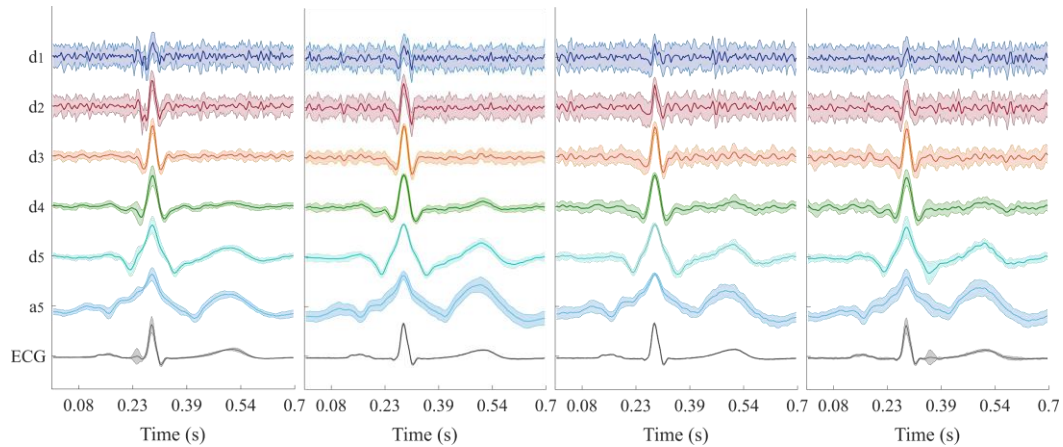
Figure 5-4. Averaged PQRST over the heartbeats for d_1- d_5 and a_5 for Rest and C_1-C_3 (from left to right).

criterion was set to the functional *CC* of the averaged PQRST of Lead II and the selected Zephlet feature.

5.2.4 Robustness of the Mother Wavelet

The optimized mother wavelet would potentially be subject-specific. Therefore, the optimization procedure was first done for each subject individually. In addition, the optimally designed mother wavelet for Rest may not be optimal for *EF* conditions and vice-versa. Therefore, the optimization procedure was done separately for Rest and C_1-C_3. Further, to investigate the generalizing ability of a potential one-size-fits-all mother, we investigated the variability of the optimized mother wavelets obtained from different trials, subjects, and conditions and assessed the performance of a single generalized mother wavelet independent of the subject, trial, or noise level.

5.3 Results

5.3.1 Feature Selection

An example of the averaged PQRST from Lead II (in black), along with the averaged PQRST from different Zephlet features applied on the synthesized ECG for Rest and C_1-C_3 are illustrated in Figure 5-4. The shaded area represents the STD. The average of the functional CC of d_1-d_5 and a_5 across trials and subjects for Rest was 0. 19 ± 0.09, 0.36 ± 0.07, 0.63 ± 0.07, 0.74 ± 0.04, 0.65 ± 0.07, and 0.46 ± 0.09. Therefore, the component with the highest functional CC was identified as d4 for Rest, with a frequency range of 8-16 Hz. The same conclusion was achieved for C_1-C_3 by the functional CC of 0.73 ± 0.06, 0.72 ± 0.08, and 0.70 ± 0.09 for d4. Therefore, d4 was chosen as the best feature for further processing steps.

5.3.2 Mother Wavelet Optimization

The mother wavelet with the maximum performance was identified for individual subjects at each condition. The corresponding zero-phased lowpass and highpass filters are represented in colour in Figure 5-5 for Rest and C_1-C_3 conditions. We used 3-fold cross-validation to evaluate the performance of the parametrized mother wavelets and choose the one with the maximum performance in the training dataset. The CC between the averaged PQRST from Lead II and d4 using these optimized mother wavelets for individual subjects
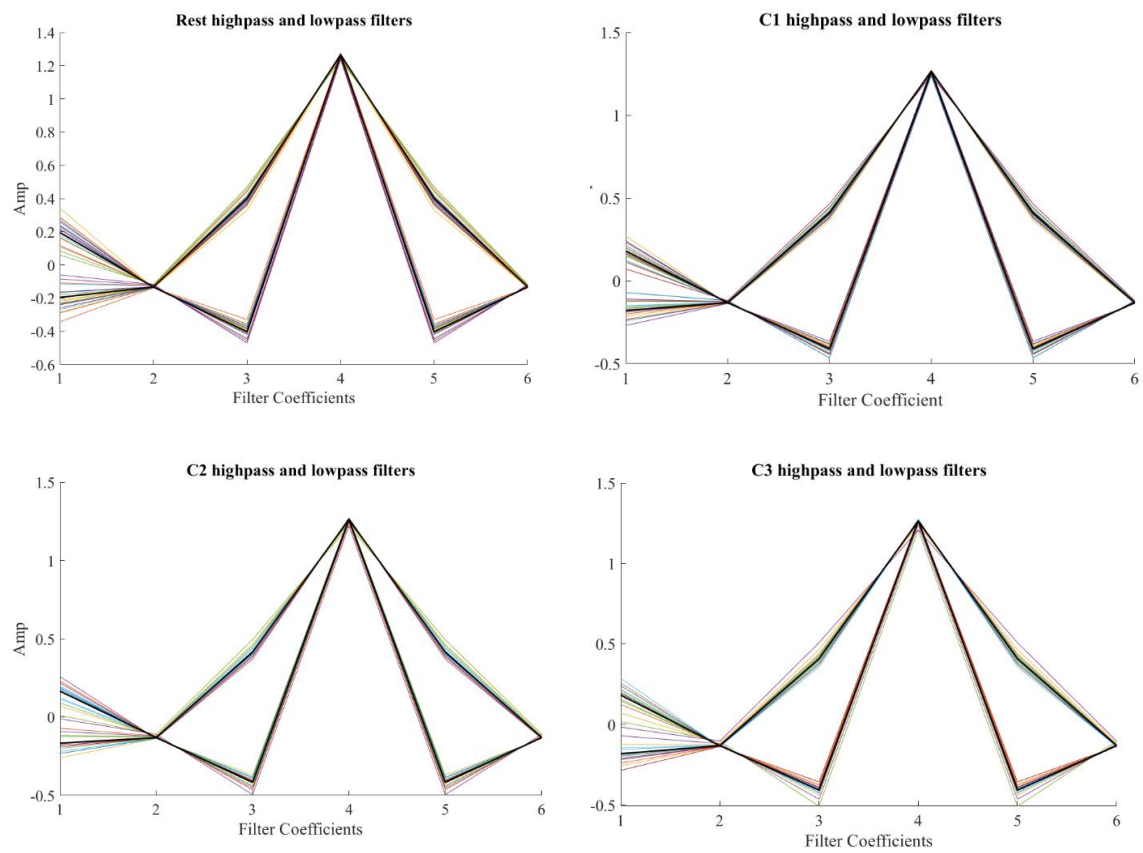
Figure 5-5. The optimized highpass and howpass filters for individual subjects at rest and the three muscle contraction level (C_1-C_3). The black line for each level represents the filters with the highest performance averaged on the subjects.

(averaged over trials and folds) in the test dataset was 0.88 ± 0.05, 0.85 ± 0.08, 0.83 ± 0.11, and 0.81 ± 0.1 for Rest and C_1-C_3, respectively as shown in Figure 5-6.

The robustness of the designed mother wavelet to EMG interference is crucial in any
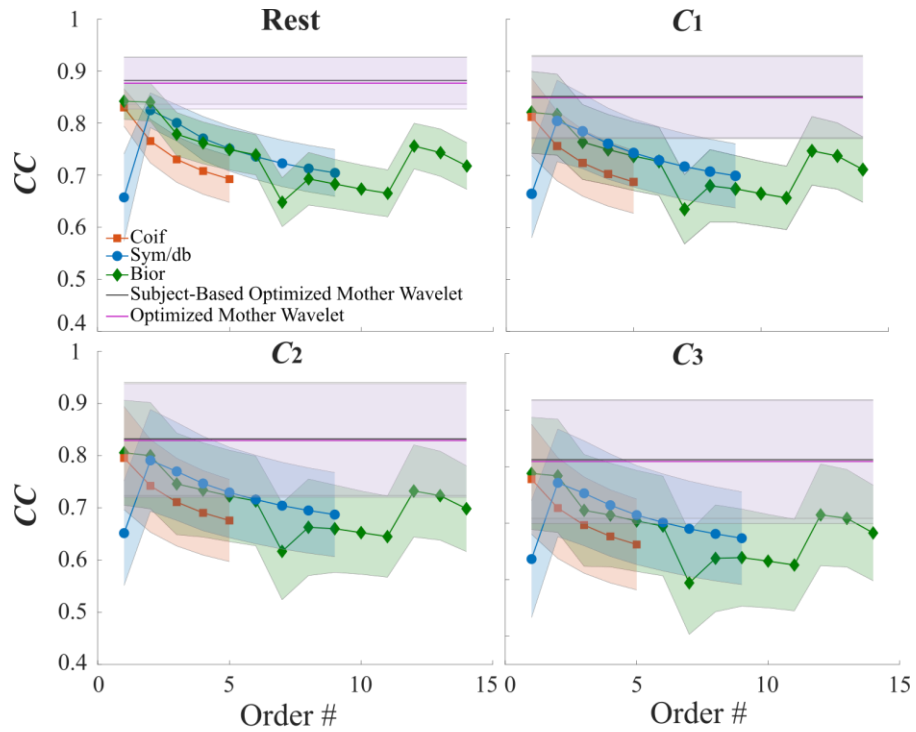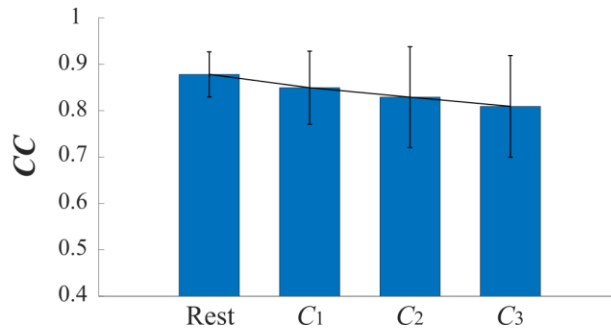
Figure 5-6. Top: The functional *CC* of the averaged PQRST over the heartbeats from LeadII and d4 (from Zephlet) for Rest and C_1-C_3. As illustrated, the optimized mother wavelet performs better compared to all different order numbers of various conventional mother wavelets. The most competitive mother wavelet is bior 1.3 in Rest and C_1-C_3. Bottom: The robustness of optimized mother wavelet performance against EMG intensity level increment.

98

further practical applications. Therefore, the ideal case would be using one mother wavelet for PQRST delineation, regardless of the EMG interference levels. Therefore, we investigated the performance of the optimized mother wavelet from Rest for the other conditions (C_1-C_3). Compared to using the corresponding optimized mother wavelet for each condition, there was no significant difference in functional CC ($p > 0.05$). Moreover, each of the optimized mother wavelets from C_1-C_3 provided us with the same performance in other muscle contraction levels ($p > 0.05$) and Rest ($p > 0.01$). Therefore, not only could we generalize the mother wavelet across subjects, but also we generalized it across various muscle contraction levels. Moreover, by an insightful observation, we realized that the generalized mother wavelet for C_2 and C_3 were identical.

5.4 Discussions

Accurately identifying cardiac arrhythmias can prevent many deaths related to these conditions. Wearable devices can provide long-term continuous cardiac monitoring by acquiring cardiac electrical activity on the body surface from non-conventional electrode placement without the intervention of clinical staff. Analyzing the acquired data allows the identification of cardiac arrhythmias [1]. The information that is required for such identification includes the location of heartbeats and their morphology.

Our previous study was designed for heartbeat detection using the signals recorded from the upper arm. We first identified the optimal electrode locations on the upper arm through

99

high-density surface recording (a total of 192 electrodes) and generated a synthesized ECG using those. Next, we detected heartbeats from synthesized ECG using Zephlet incorporated with a Multiagent Detection Scheme (*MDS*).

The present study was designed for ECG delineation using the signals recorded from the upper arm. Following our previous study, we initially generated the synthesized ECG and extracted a number of Zephlet features (d_1-d_5, a_5). We first selected a Zephlet feature with the most similarity to PQRST. Next, we optimized the mother wavelet to further improve PQRST delineation performance from the selected feature, for each individual and at each muscle contraction level. Following that, we investigated the possibility of generalizing an optimized mother wavelet across all the subjects and conditions. Finally, we compared the PQRST delineation performance of the optimized mother wavelet to the conventional mother wavelet families for a better selection of a mother wavelet that works best for this criterion.

With respect to the first question, we identified d4 (8-16 Hz) as the most informative Zephlet component. Many wavelet-based ECG processing studies have focused on the selection of a wavelet component that provides the most information. The selected details include 2 (31.25-62.5 Hz) [62], 3-5 (5.75-45 Hz) [2], and 4 (15.6-31.1 Hz) [63], which represent a higher frequency range than our selected detail. However, it should be mentioned that these frequency ranges were selected for QRS detection while we were targeting PQRST delineation. Therefore, the inclusion of lower frequency ranges plays an important role in this

application. Some of the above studies have also selected details with a lower frequency range for P- and T-wave delineation [2][61].

Focusing on the second research question, we parametrized the mother wavelet using the Lattice parametrization method introduced by Vaidyanathan [100]. Therefore, we were able to generate 361 different mother wavelets and select the highest-performing one for individual subjects in each condition. We identified a single mother wavelet from the 361 candidates for all subjects without a significant loss in the overall performance in each condition. Moreover, we investigated the possibility of further generalizing the mother wavelet over different conditions *i.e.* Rest and different levels of *EF*. The results led us to the most important finding of this study, which is achieving a generalized mother wavelet for PQRST delineation that can be used for all participants and conditions.

Comparing the results of the optimized mother wavelet with the conventional wavelet families represents the advantage of the proposed method. Among the conventional wavelet families, Bior1.3 had the best performance. Although many studies have investigated the selection of a mother wavelet with the highest performance for QRS delineation in the literature, the results include a wide range of mother wavelets, including Bior 2.6 [101], Haar [76], Sym4 [102], and db9 [77]. The different results from the literature suggested that selecting an optimized mother wavelet for QRS detection, which is highly important in detecting arrhythmias, has remained an open issue. It is worth noting that similar to our

101

findings, Kher et al. identified Bior 3.7 as the best mother wavelet for ECG reconstruction during various physical activities, in which case the ECG recording had low SNR [103]. The generalized Zephlet mother wavelet we reported in the current study is robust to noise level and subject-independent. It is especially valuable in extracting vital cardiac information using wearable devices during daily activities of living.

This study has some limitations. Firstly, the generalisability of the presented results is limited by the relatively small participant pool and the contractions of only the biceps brachii muscle. A natural progression of this work is to include various arm movements and activities and investigate the optimized mother wavelet performance over a larger number of participants. On the other hand, because of the different morphologies and structures of the heart, the ECG signal of each individual possesses a unique pattern, particularly for patients with cardiac conditions. Although the generalization of mother wavelet over subjects helps with eliminating individual-based training, the variation among subjects will be missed. The same holds for the heartbeat morphologies as well because of their time-varying nature. Moreover, despite the promising results of this algorithm, the location of heartbeats is considered known. The overall performance of PQRST delineation using the optimized mother wavelet combined with our heartbeat detection algorithm from the previous study [98] would be the next step of this study. Lastly, a single mother wavelet and a single Zephlet component (d4) were used in the delineation of all P-wave, QRS complex, and T-wave. In future

investigations, it would be desirable to delineate the QRS complex, P-wave and T-wave, using different components, as the three waves have different frequency ranges, as discussed in the literature [2][61]. Such a scheme can be implemented by allocating a particular waveform in the resulting PQRST to the one extracted from its corresponding component.

Chapter 6

Conclusion

6.1 Summary and Concluding Remarks

Real-time cardiac activity monitoring is crucial for people with sensitive heart conditions such as arrhythmias. Extracting cardiac information that represents the heart activity is required to achieve constant cardiac monitoring. However, conventional standard chest ECG recording suffers from inconveniency, additional wires, and low wearability. Therefore, extracting cardiac information from the electrodes placed on the upper arm with higher wearability and comfort is an alternative approach proposed in this study. Toward this goal, an experiment was designed to acquire Lead II simultaneously with signals recorded from the upper arm using 192 high-density EMG electrodes. The experiment included two conditions: Rest and *EF,* at which the participants hold different weights (C_1:1.2 kg, C_2: 2.2 kg, C_3: 3.6 kg) that generates various EMG activity levels.

The importance of this thesis lies in the precise extraction of heartbeat locations and delineation of ECG waveforms using the signals recorded from the upper arm. The findings make several contributions to the current literature. First, we identified the precise optimal location of a pair of electrodes on the upper arm for heartbeat detection at Rest and *EF* conditions (C_1-C_3). Next, we introduced consistent spatial filter weights (across subjects,

conditions, and trials) for these electrodes in order to generate a synthesized ECG with the highest similarity to Lead II, which is critical for generalization purposes. Furthermore, after identifying SWT as a robust algorithm against EMG increment compared to state-of-the-art methods, we addressed two important SWT drawbacks: phase shift and pre-defined mother wavelet requirement. Focusing on phase shift elimination, we used Zephlet incorporated with *MDS* for heartbeat detection and reported the results at different tolerance levels. The results of Zephlet were compared to SWT to emphasize the importance of eliminating the phase shift that SWT causes in feature extraction. Next, we designed a mother wavelet that was specifically optimized to delineate PQRST waveforms for each subject and EMG intensity level. We then went one step further and optimized a mother wavelet that can be generalized over subjects and EMG intensity levels. This designed mother wavelet can be further used in many applications that utilize WT for the extraction of ECG information. Accordingly, the second SWT drawback was also addressed, resulting in significantly better ECG delineation performance than conventional mother wavelets. The identified electrode locations, generalized weights, proposed heartbeat detection algorithm using Zephlet, and optimized mother wavelet can be further used in wearable devices for the purpose of extracting cardiac information.

6.2 Limitations and Future Work

This thesis has some main limitations. Firstly, the generalisability of the presented results is limited by the relatively small participant pool and the contractions of only the biceps brachii muscle. A natural progression of this work is to include more participants and various arm movements and activities. Moreover, for the algorithms to be implementable in wearable devices, we have generalized the location and the weight of electrodes on the upper arm. Therefore, we are not using the most informative channels and the best weights for each individual. Similarly, although the generalization of mother wavelet over subjects helps with eliminating individual-based training, the variation among subjects will be missed. The same holds for the heartbeat morphologies detection using a generalized mother wavelet because of their time-varying nature. In addition, the optimized mother wavelet can be tailored for different arrhythmias, which helps with arrhythmia detection applications. And lastly, the heartbeat detection methodology that is used in this thesis is the popular Pan-Tompkins algorithm [83][96]. Despite the promising results of this algorithm, alternative detection algorithms should be investigated in the future.

References

[1]   Z. Jin, J. Oresko, S. Huang, and A. C. Cheng, "HeartToGo: A personalized medicine technology for cardiovascular disease prevention and detection," in *IEEE/NIH Life Science Systems and Applications Workshop*, 2009, pp. 80–83.

[2]   S. Z. Mahmoodabadi, A. Ahmadian, M. D. Abolhasani, M. Eslami, and J. H. Bidgoli, "ECG feature extraction based on multiresolution wavelet transform," in *Annual International Conference of the IEEE Engineering in Medicine and Biology - Proceedings*, 2005, vol. 7 VOLS, pp. 3902–3905.

[3]   C. Areia *et al.*, "Experiences of current vital signs monitoring practices and views of wearable monitoring: A qualitative study in patients and nurses," *J. Adv. Nurs.*, vol. 78, no. 3, pp. 810–822, Mar. 2022.

[4]   L. Salvaraji, M. S. Jeffree, K. Awang Lukman, S. Saupin, and R. Avoi, "Electrical safety in a hospital setting: A narrative review," *Ann. Med. Surg.*, vol. 78, p. 103781, Jun. 2022.

[5]   Q. Zhang and D. Zhou, "Deep arm/ear-ECG image learning for highly wearable biometric human identification," *Ann. Biomed. Eng.*, vol. 46, no. 1, pp. 122–134, 2018.

[6]   A. Soroudi, N. Hernández, L. Berglin, and V. Nierstrasz, "Electrode placement in electrocardiography smart garments: A review," *Journal of Electrocardiology*, vol. 57.

Churchill Livingstone Inc., pp. 27–30, 01-Nov-2019.

[7]   A. Lourenço, H. Silva, and A. Fred, "Unveiling the biometric potential of finger-based ECG signals," *Comput. Intell. Neurosci.*, vol. 2011, 2011.

[8]   W. D. Lynn, O. J. Escalona, and D. J. McEneaney, "Arm and wrist surface potential mapping for wearable ECG rhythm recording devices: A pilot clinical study," *J. Phys. Conf. Ser.*, vol. 450, no. 1, 2013.

[9]   C. J. Harland, T. D. Clark, and R. J. Prance, "High resolution ambulatory electrocardiographic monitoring using wrist-mounted electric potential sensors," *Meas. Sci. Technol.*, vol. 14, no. 7, pp. 923–928, 2003.

[10]   O. J. Escalona, W. D. Lynn, G. Perpiñan, L. McFrederick, and D. J. McEneaney, "Data-driven ECG denoising techniques for characterising bipolar lead sets along the left arm in wearable long-term heart rhythm monitoring," *Electron.*, vol. 6, no. 4, 2017.

[11]   D. H. Peter Sam Raj, "Feasibility of single-arm single-lead ECG biometrics," in *22nd European Signal Processing Conference (EUSIPCO)*, 2014, pp. 2525–2529.

[12]   Q. Zhang, D. Zhou, and X. Zeng, "Highly wearable cuff-less blood pressure and heart rate monitoring with single-arm electrocardiogram and photoplethysmogram signals," *Biomed. Eng. Online*, vol. 16, no. 1, pp. 1–20, 2017.

[13]   S. Schuler, D. Potyagaylo, and D. Olaf, "Using a spatio-temporal basis for ECG imaging

of ventricular pacings : insights from simulations and first application to clinical data," in *1st Annual International Conference of the IEEE Engineering in Medicine and Biology Society (EMBC)*, 2019, pp. 1559–1562.

[14] M. D. Ivanovic, M. Miletic, I. Subotic, and D. Boljevic, "Signal quality in reconstructed 12-lead ambulatory ECGs recorded using 3-lead device," in *41st Annual International Conference of the IEEE Engineering in Medicine & Biology Society (EMBC)*, 2019, pp. 5481–5487.

[15] V. Jeyhani, M. Matti, K. Noponen, T. Sepp, and A. Vehkaoja, "Effect of different ECG leads on estimated R-R intervals and heart rate variability parameters," in *1st Annual International Conference of the IEEE Engineering in Medicine and Biology Society (EMBC)*, 2019, pp. 3786–3790.

[16] N. Spicher and M. Kukuk, "ECG delineation using a piecewise Gaussian derivative model with parameters estimated from scale-dependent algebraic expressions," in *41st Annual International Conference of the IEEE Engineering in Medicine and Biology Society (EMBC)*, 2019, pp. 5633–5637.

[17] M. C. Gibson *et al.*, "Diagnostic and prognostic value of ambulatory ECG (Holter) monitoring in patients with coronary heart disease: A review," *Journal of Thrombosis and Thrombolysis*, vol. 23, no. 2. pp. 135–145, Apr-2007.

[18] C. L. Karmen, M. A. Reisfeld, M. K. McIntyre, R. Timmermans, and W. Frishman,

"The clinical value of heart rate monitoring using an Apple Watch," *Cardiol. Rev.*, vol. 27, no. 2, pp. 60–62, 2019.

[19]   F. Liu *et al.*, "Performance Analysis of Ten Common QRS Detectors on Different ECG Application Cases," *J. Healthc. Eng.*, vol. 2018, 2018.

[20]   M. Merah, T. A. Abdelmalik, and B. H. Larbi, "R-peaks detection based on stationary wavelet transform," *Comput. Methods Programs Biomed.*, vol. 121, no. 3, pp. 149–160, 2015.

[21]   E. McAdams *et al.*, "Wearable electronic systems: Applications to medical diagnostics/monitoring," in *Wearable Monitoring Systems*, Springer US, 2011, pp. 179–203.

[22]   J. Enderle and B. Joseph, *Introduction to biomedical engineering*. Academic Press, 2012.

[23]   G. D. Clifford, F. Azuaje, and P. E. McSharry, *Advanced methods and tools for ECG data analysis*. Artech house, 2006.

[24]   A. Ricardo *et al.*, "The enigmatic sixth wave of the electrocardiogram: The U wave," *Cardiol. J.*, vol. 15, no. 5, pp. 408–421, 2008.

[25]   A. Gacek and W. Pedrycz, *ECG Signal Processing, Classification and Interpretation: A Comprehensive Framework of Computational Intelligence*. 2011.

[26]   M. Abdelazez, S. Rajan, and A. D. Chan, "Detection of noise type in Electrocardiogram," in *MeMeA 2018 - 2018 IEEE International Symposium on Medical Measurements and Applications, Proceedings*, 2018.

[27]   H. Limaye and V. V. Deshmukh, "ECG noise sources and various noise removal techniques: a survey," *Int. J. Appl. or Innov. Eng. Manag.*, vol. 5, no. 2, 2016.

[28]   S. A. Israel, J. M. Irvine, A. Cheng, M. D. Wiederhold, and B. K. Wiederhold, "ECG to identify individuals," *Pattern Recognit.*, vol. 38, no. 1, pp. 133–142, Jan. 2005.

[29]   M. Phegade and P. Mukherji, "ICA based ECG signal denoising," in *International Conference on Advances in Computing, Communications and Informatics (ICACCI)*, 2013.

[30]   I. Romero, "PCA and ICA applied to noise reduction in multi-lead ECG," in *Computing in Cardiology*, 2011, pp. 613–616.

[31]   K. C. Mcgill, "Surface electromyogram signal modelling," *Med. Biol. Eng. Comput.*, vol. 42, no. 4, pp. 446–454, 2004.

[32]   P. A. Kaplanis, C. S. Pattichis, L. J. Hadjileontiadis, and V. C. Roberts, "Surface EMG analysis on normal subjects based on isometric voluntary contraction," *J. Electromyogr. Kinesiol.*, vol. 19, no. 1, pp. 157–171, Feb. 2009.

[33]   G. Kamen and G. David, *Essentials of electromyography: human kinetics*. Canada:

Human Kinetics, 2010.

[34] W. D. Lynn, O. J. Escalona, and D. J. McEneaney, "ECG monitoring techniques using advanced signal recovery and arm worn sensors," *2014 IEEE Int. Conf. Bioinforma. Biomed. IEEE BIBM 2014*, pp. 51–55, Dec. 2014.

[35] F. Liu *et al.*, "Performance analysis of ten common QRS detectors on different ECG application cases," *J. Healthc. Eng.*, vol. 2018, 2018.

[36] P. Hong, J. Hsiao, C. Chung, Y. Feng, and S. W. Member, "ECG biometric recognition : template-free approaches based on deep learning," *41st Annu. Int. Conf. IEEE Eng. Med. Biol. Soc.*, pp. 2633–2636, 2019.

[37] J. Fraden and M. R. Neuman, "QRS wave detection," *Med. Biol. Eng. Comput.*, vol. 18, no. 2, pp. 125–132, Mar. 1980.

[38] M. Elgendi, B. Eskofier, S. Dokos, and D. Abbott, "Revisiting QRS detection methodologies for portable, wearable, battery-operated, and wireless ECG systems," *PLoS One*, vol. 9, no. 1, Jan. 2014.

[39] F. Sufi, Q. Fang, and I. Cosic, "ECG R-R peak detection on mobile phones," in *Annual International Conference of the IEEE Engineering in Medicine and Biology*, 2007, pp. 3697–3700.

[40] M. Okada, "A digital filter for the QRS complex detection," *IEEE Trans. Biomed. Eng.*,

vol. BME-26, no. 12, pp. 700–703, 1979.

[41] N. M. Arzeno, Z.-D. Deng, and C.-S. Poon, "Analysis of first-derivative based QRS detection algorithms," *IEEE Trans. Biomed. Eng.*, 2008.

[42] M. L. Ahlstrom and W. J. Tompkins, "Automated high-speed analysis of holter tapes with microcomputers," *IEEE Trans. Biomed. Eng.*, vol. BME-30, no. 10, pp. 651–657, 1983.

[43] I. I. Christov and I. K. Daskalov, "Filtering of electromyogram artifacts from the electrocardiogram," *Med. Eng. Phys.*, vol. 21, no. 10, pp. 731–736, 1999.

[44] N. E. Huang *et al.*, "The empirical mode decomposition and the Hubert spectrum for nonlinear and non-stationary time series analysis," *Proc. R. Soc. A Math. Phys. Eng. Sci.*, vol. 454, no. 1971, pp. 903–995, 1998.

[45] M. Rakshit and S. Das, "An efficient ECG denoising methodology using empirical mode decomposition and adaptive switching mean filter," *Biomed. Signal Process. Control*, vol. 40, pp. 140–148, 2018.

[46] C. Kozia, R. Herzallah, and D. Lowe, "ECG-derived respiration using a real-time qrs detector based on empirical mode decomposition," in *12th International Conference on Signal Processing and Communication Systems, ICSPCS 2018*, 2018, pp. 1–8.

[47] H. Xing and M. Huang, "A new QRS detection algorithm based on empirical mode

decomposition," in *2nd International Conference on Bioinformatics and Biomedical Engineering, iCBBE 2008*, 2008, pp. 693–696.

[48] K. Yannis and M. Stephen, "Development of EMD-Based Denoising Methods Inspired by Wavelet Thresholding," *IEEE Trans. Signal Process.*, pp. 1351–1362, 2009.

[49] L. El Bouny, M. Khalil, and A. Adib, "Performance analysis of ECG signal denoising methods in transform domain," in *2018 International Conference on Intelligent Systems and Computer Vision, ISCV 2018*, 2018, vol. 2018-May, pp. 1–8.

[50] W. Mohguen and R. E. H. Bekka, "EMD-based denoising by customized thresholding," in *2017 International Conference on Control, Automation and Diagnosis, ICCAD 2017*, 2017, pp. 19–23.

[51] X. Xiaomin and L. Ying, "Adaptive threshold for QRS complex detection based on wavelet transform," in *Annual International Conference of the IEEE Engineering in Medicine and Biology*, 2005, vol. 7 VOLS, pp. 7281–7284.

[52] A. Safari, H. D. Hesar, M. Mohebbi, and F. Faradji, "A novel method for R-peak detection in noisy ECG signals using EEMD and ICA," in *2016 23rd Iranian Conference on Biomedical Engineering and 2016 1st International Iranian Conference on Biomedical Engineering, ICBME 2016*, 2017, pp. 155–158.

[53] N. Abdolmaleki and M. Pooyan, "Source separation from single channel biomedical

signal by combination of blind source separation and empirical mode decomposition," *Int. J. Digit. Inf. Wirel. Commun.*, vol. 2, no. 1, pp. 75–82, Jan. 2012.

[54] B. Mijović, M. De Vos, I. Gligorijević, J. Taelman, and S. Van Huffel, "Source separation from single-channel recordings by combining empirical-mode decomposition and independent component analysis," *IEEE Trans. Biomed. Eng.*, vol. 57, no. 9, pp. 2188–2196, Sep. 2010.

[55] Z. Wu and N. E. Huang, "Ensemble empirical mode decomposition: A noise-assisted data analysis method," *Adv. Adapt. Data Anal.*, vol. 1, no. 1, pp. 1–41, Jan. 2009.

[56] G. Han, B. Lin, and Z. Xu, "Electrocardiogram signal denoising based on empirical mode decomposition technique: an overview," *J. Instrum.*, vol. 12, p. P03010, 2016.

[57] L. El Bouny, M. Khalil, and A. Adib, "ECG signal denoising based on ensemble emd thresholding and higher order statistics," in *3rd International Conference on Advanced Technologies for Signal and Image Processing, ATSIP 2017*, 2017.

[58] S. Zhang, J. Tian, A. Banerjee, and J. Li, "An efficient porcine acoustic signal denoising technique based on EEMD-ICA-WTD," *Math. Probl. Eng.*, vol. 2019, 2019.

[59] M. E. Torres, M. A. Colominas, G. Schlotthauer, and P. Flandrin, "A complete ensemble empirical mode decomposition with adaptive noise," in *ICASSP, IEEE International Conference on Acoustics, Speech and Signal Processing - Proceedings*, 2011, pp. 4144–

4147.

[60] S. Raj, K. C. Ray, and O. Shankar, "Development of robust, fast and efficient QRS complex detector: a methodological review," *Australasian Physical and Engineering Sciences in Medicine*, vol. 41, no. 3. Springer Netherlands, pp. 581–600, 2018.

[61] J. P. Martínez, R. Almeida, S. Olmos, A. P. Rocha, and P. Laguna, "A wavelet-based ECG delineator evaluation on standard databases," *IEEE Trans. Biomed. Eng.*, vol. 51, no. 4, pp. 570–581, Apr. 2004.

[62] V. X. Afonso, W. J. Tompkins, T. Q. Nguyen, and S. Luo, "ECG beat detection using filter banks," *IEEE Trans. Biomed. Eng.*, vol. 46, no. 2, pp. 192–202, 1999.

[63] S. C. Saxena, V. Kumar, and S. T. Hamde, "Feature extraction from ECG signals using wavelet transforms for disease diagnostics," *Int. J. Syst. Sci.*, vol. 33, pp. 1073–1085, 2002.

[64] S. Mallat and W. L. Hwang, "Singularity detection and processing with wavelets," *IEEE Trans. Inf. Theory*, vol. 38, no. 2, pp. 617–643, 1992.

[65] X. Zheng, L. Shen, Z. Li, and Z. Ji, "Detection of QRS complexes based on biorthogonal spline wavelet," in *2008 International Symposium on Information Science and Engineering, ISISE 2008*, 2008, vol. 2, pp. 502–506.

[66] D. Labate, F. La Foresta, G. Occhiuto, F. C. Morabito, A. Lay-Ekuakille, and P.

Vergallo, "Empirical mode decomposition vs. wavelet decomposition for the extraction of respiratory signal from single-channel ECG: A comparison," *IEEE Sens. J.*, vol. 13, no. 7, pp. 2666–2674, 2013.

[67] S. Pal and M. Mitra, "Empirical mode decomposition based ECG enhancement and QRS detection," *Comput. Biol. Med.*, vol. 42, no. 1, pp. 83–92, 2012.

[68] M. Mendez *et al.*, "Automatic screening of obstructive sleep apnea from the ECG based on empirical mode decomposition and wavelet analysis Related content," *Physiol. Meas. Autom.*, pp. 273–289, 2010.

[69] G. Lenis, N. Pilia, T. Oesterlein, A. Luik, C. Schmitt, and O. Dössel, "P wave detection and delineation in the ECG based on the phase free stationary wavelet transform and using intracardiac atrial electrograms as reference," *Biomed. Eng. / Biomed. Tech.*, vol. 61, no. 1, pp. 37–56, Feb. 2016.

[70] G. Baldazzi, E. Sulas, M. Urru, R. Tumbarello, L. Raffo, and D. Pani, "Wavelet denoising as a post-processing enhancement method for non-invasive foetal electrocardiography," *Comput. Methods Programs Biomed.*, vol. 195, p. 105558, Oct. 2020.

[71] A. Kumar, H. Tomar, V. K. Mehla, R. Komaragiri, and M. Kumar, "Stationary wavelet transform based ECG signal denoising method," *ISA Trans.*, vol. 114, pp. 251–262, Aug. 2021.

[72] N. Heydari Beni and N. Jiang, "Heartbeat detection from the upper arm using an SWT-based zero-phase filter bank incorporated with a voting scheme," in *44st Annual International Conference of the IEEE Engineering in Medicine & Biology Society (EMBC)*, 2022.

[73] D. Percival, "Discrete wavelet transforms based on zero-phase Daubechies filters," in *Info-Metrics Institute Conference, http://faculty.washington.edu/dbp/PDFFILES/zephlet*, 2010.

[74] D. B. Percival and Walden Andrew T., *Wavelet methods for time series analysis*. Cambridge university press, 2000.

[75] M. A. Motin, C. K. Karmakar, and M. Palaniswami, "Ensemble empirical mode decomposition with principal component analysis: a novel approach for extracting respiratory rate and heart rate from photoplethysmographic signal," *IEEE J. Biomed. Heal. Informatics*, vol. 22, no. 3, pp. 766–774, May 2018.

[76] A. A. R. Bsoul, S. Y. Ji, K. Ward, and K. Najarian, "Detection of P, QRS, and T components of ECG using wavelet transformation," *2009 ICME Int. Conf. Complex Med. Eng. C. 2009*, 2009.

[77] U. Seljuq, F. Himayun, and H. Rasheed, "Selection of an optimal mother wavelet basis function for ECG signal denoising," in *17th IEEE International Multi Topic Conference*, 2014, pp. 26–30.

[78] M. Vollmer, "Robust detection of heart beats using dynamic thresholds and moving windows," *Comput. Cardiol. (2010).*, 2014.

[79] S. Banerjee and M. Mitra, "Application of cross wavelet transform for ECG pattern analysis and classification," *IEEE Trans. Instrum. Meas.*, vol. 63, no. 2, pp. 326–333, 2014.

[80] B. N. Singh and A. K. Tiwari, "Optimal selection of wavelet basis function applied to ECG signal denoising," *Digit. Signal Process. A Rev. J.*, vol. 16, no. 3, pp. 275–287, May 2006.

[81] P. Morizet-Mahoudeaux, C. Moreau, D. Moreau, and J. J. Quarante, "Simple microprocessor-based system for on-line e.c.g. arrhythmia analysis," *Med. Biol. Eng. Comput.*, vol. 19, no. 4, pp. 497–500, 1981.

[82] G. M. Friesen, T. C. Jannett, M. A. Jadallah, S. L. Yates, S. R. Quint, and H. T. Nagle, "A Comparison of the Noise Sensitivity of Nine QRS Detection Algorithms," *IEEE Trans. Biomed. Eng.*, vol. 37, no. 1, pp. 85–98, 1990.

[83] J. Pan and W. J. Tompkins, "A comparison of the noise sensitivity of nine QRS detection algorithms," *IEEE Trans. Biomed. Eng.*, vol. BME-32, no. 3, pp. 230–236, 1985.

[84] B. U. Kohler, C. Hennig, and R. Orglmeister., "QRS detection using zero crossing counts," *Prog. Biomed. Res.*, vol. 8, no. 3, pp. 138–145, 2003.

[85] L. Shyu, Y. Wu, W. H.-I. T. on Biomedical, and U. 2004, "Using wavelet transform and fuzzy neural network for VPC detection from the Holter ECG," *IEEE Trans. Biomed. Eng.*, vol. 51, no. 7, pp. 1269–1273, 2004.

[86] D. T. Kaplan, "Simultaneous QRS detection and feature extraction using simple matched filter basis functions," in *Computers in Cardiology*, 1991, pp. 503–506.

[87] G. B. Moody and R. G. Mark, "The impact of the MIT-BIH arrhythmia database," *IEEE Engineering in Medicine and Biology Magazine*, vol. 20, no. 3. pp. 45–50, 2001.

[88] P. McCool, G. D. Fraser, A. D. C. Chan, L. Petropoulakis, and J. J. Soraghan, "Identification of contaminant type in surface electromyography (EMG) signals," *IEEE Trans. Neural Syst. Rehabil. Eng.*, 2014.

[89] E. Shwedyk, R. Balasubramanian, and R. Scott, "A nonstationary model for the electromyogram," *IEEE Trans. Biomed. Eng.*, 1997.

[90] D. Farina and R. Merletti, "Comparison of algorithms for estimation of EMG variables during voluntary isometric contractions," *J. Electromyogr. Kinesiol.*, vol. 10, no. 5, pp. 337–349, Oct. 2000.

[91] D. Langlois, S. Chartier, and D. Gosselin, "An Introduction to Independent Component Analysis: InfoMax and FastICA algorithms," *Tutor. Quant. Methods Psychol.*, vol. 6, no. 1, pp. 31–38, 2010.

[92] A. Bin Queyam, † Id, S. Kumar Pahuja, and D. Singh, "Quantification of Feto-Maternal Heart Rate from Abdominal ECG Signal Using Empirical Mode Decomposition for Heart Rate Variability Analysis," *Technol. 2017, Vol. 5, Page 68*, vol. 5, no. 4, 2017.

[93] M. B. Hossain, S. K. Bashar, A. J. Walkey, D. D. McManus, and K. H. Chon, "An accurate QRS complex and P wave detection in ECG signals using complete ensemble empirical mode decomposition with adaptive noise approach," *IEEE Access*, vol. 7, pp. 128869–128880, 2019.

[94] A. K. Dwivedi, H. Ranjan, A. Menon, and P. Periasamy, "Noise reduction in ECG signal using combined ensemble empirical mode decomposition method with stationary wavelet transform," *Circuits, Syst. Signal Process.*, vol. 40, no. 2, pp. 827–844, Feb. 2021.

[95] M. Marouf, L. Saranovac, and G. Vukomanovic, "Algorithm for EMG noise level approximation in ECG signals," *Biomed. Signal Process. Control*, vol. 34, pp. 158–165, Apr. 2017.

[96] N. Heydari Beni and N. Jiang, "Heartbeat detection from a single-lead ECG contaminated with simulated EMG at different intensity levels: a comparative study," *Biomed. Signal Process. Control*, Jan. 2023.

[97] J. Pan and W. J. Tompkins, "A Real-Time QRS Detection Algorithm," *IEEE Trans. Biomed. Eng.*, vol. BME-32, no. 3, pp. 230–236, 1985.

[98] N. Heydari Beni and N. Jiang, "Heartbeat detection from high-density EMG electrodes on the upper arm at different EMG intensity levels using Zephlet," *SSRN Electron. J.*, Oct. 2022.

[99] D. Farina, M. F. Lucas, and C. Doncarli, "Optimized wavelets for blind separation of nonstationary surface myoelectric signals," *IEEE Trans. Biomed. Eng.*, vol. 55, no. 1, pp. 78–86, 2008.

[100] P. P. Vaidyanathan, *Multirate systems and filter banks*. Pearson Education India, 2006.

[101] M. M. Tantawi, K. Revett, A. B. Salem, and M. F. Tolba, "A wavelet feature extraction method for electrocardiogram (ECG)-based biometric recognition," *Signal, Image Video Process.*, vol. 9, no. 6, pp. 1271–1280, Sep. 2015.

[102] B. Castro, D. Kogan, and A. B. Geva, "ECG feature extraction using optimal mother wavelet," in *21st IEEE Convention of the Electrical and Electronic Engineers in Israel. Proceedings (Cat. No. 00EX377)*, 2000, pp. 346–350.

[103] R. Kher, T. Pawar, V. Thakar, and H. Shah, "Physical activities recognition from ambulatory ECG signals using neuro-fuzzy classifiers and support vector machines," *http://dx.doi.org/10.3109/03091902.2014.998372*, vol. 39, no. 2, pp. 138–152, Feb. 2015.